1 **Single-cell profiling and SCOPE-seq reveal the lineage dynamics of adult neurogenesis**

2 **and NOTUM as a key V-SVZ regulator**

3

4 Dogukan Mizrak[1], N. Sumru Bayin[2], Jinzhou Yuan[1], Zhouzerui Liu[1], Radu Suciu[3], Micah J.

5 Niphakis[4], Nhi Ngo[4], Kenneth M. Lum[4], Benjamin F. Cravatt[3], Alexandra L. Joyner[2,5], Peter A.

6 Sims[1*]

7

8 [1]*Department of Systems Biology, Biochemistry & Molecular Biophysics, Columbia University*

9 *Irving Medical Center, New York, NY 10032 USA.*

10 [2]*Developmental Biology Program, Sloan Kettering Institute, New York, NY 10065 USA.*

11 [3]*Department of Molecular Medicine, The Scripps Research Institute, La Jolla, CA 92037 USA.*

12 [4]*Lundbeck La Jolla Research Center, Inc. 10835 Road to the Cure, Suite 250, San Diego, CA*

13 *92121, USA.*

14 [5]*Biochemistry, Cell and Molecular Biology Program, Weill Cornell Graduate School of Medical*

15 *Sciences, New York, NY 10065 USA.*

16

17 *Lead Contact:

18 Peter A. Sims

19 3960 Broadway, 2nd Floor, Room 203AC

20 New York, NY 10032

21 Phone: (212) 305-2687

22 email: pas2182@cumc.columbia.edu

23

24 **SUMMARY**

25 Neural stem cells (NSCs) and their progeny reside in specialized niches in the adult mammalian

26 brain where they generate new neurons and glia throughout life. Adult NSCs of the ventricular-

27 subventricular zone (V-SVZ) are prone to rapid exhaustion; thus timely, context-dependent

28 neurogenesis demands adaptive signaling among the vast number of neighboring progenitors

29 nestled between the ventricular surface and nearby blood vessels. To dissect adult neuronal

30 lineage progression and regulation, we profiled >56,000 V-SVZ and olfactory bulb (OB) cells by

31 single-cell RNA-sequencing (scRNA-seq). Our analyses revealed the diversity of V-SVZ-derived

32 OB neurons, the temporal dynamics of lineage progression, and a key intermediate NSC

33 population enriched for expression of *Notum*, which encodes a secreted WNT antagonist. Single

34 Cell Optical Phenotyping and Expression (SCOPE-seq), a technology linking live cell imaging with

1

35   scRNA-seq, uncovered dynamic control of cell size concomitant with NSC differentiation with

36   *Notum+* NSCs at a critical size poised for cell division, and a preference of NOTUM surface binding

37   to neuronal precursors with active WNT signaling. Finally, *in vivo* pharmacological inhibition of

38   NOTUM significantly expanded neuronal precursor pools in the V-SVZ. Our findings highlight a

39   critical regulatory state during NSC activation marked by NOTUM, a secreted enzyme that

40   ensures efficient neurogenesis by preventing WNT signaling activation in NSC progeny.

41

42   **INTRODUCTION**

43   Neurogenesis persists in two principal regions of the adult mouse brain: the subgranular zone of

44   the dentate gyrus and the V-SVZ located in the walls of the lateral ventricles (Doetsch et al., 1999;

45   Fiorelli et al., 2015; Mirzadeh et al., 2008). The V-SVZ contains both quiescent (qNSCs) and

46   actively dividing NSCs (aNSCs) (Codega et al., 2014; Mich et al., 2014) with intrinsic regional

47   identities defined during embryogenesis (Fuentealba et al., 2015), generating different OB

48   interneuron subtypes or glia depending on their location (Brill et al., 2009; Delgado and Lim, 2015;

49   Kohwi et al., 2005; Lopez-Juarez et al., 2013; Merkle et al., 2014; Merkle et al., 2007; Mizrak et

50   al., 2019; Ortega et al., 2013; Zweifel et al., 2018). V-SVZ qNSCs are specialized astrocytes with

51   radial morphology (reviewed in Kriegstein and Alvarez-Buylla, 2009; Mirzadeh et al., 2008), and

52   once activated divide symmetrically, resulting in their depletion over time (Obernier et al., 2018).

53   aNSCs give rise to transit-amplifying cells (TACs), which generate neuroblasts (NBs). NBs

54   migrate via the rostral migratory stream (RMS) to the OB (Figure 1A), where they terminally

55   differentiate into interneurons. V-SVZ NSC-to-OB interneuron differentiation requires cells with a

56   broad distribution of developmental states; however, the identities and the functions of key

57   intermediate states and the gene expression programs pertinent to these transitions are unknown.

58   While recent efforts have defined OB neuron subtypes (Eng et al., 2019; Tepe et al., 2018),

59   classification of V-SVZ-derived OB neurons by fate-mapped scRNA-seq is still lacking.

60

61   Intercellular communication in the V-SVZ is essential for proper adult neurogenesis, but has not

62   been fully explored, particularly at the single-cell level. GABA released by NBs inhibits NSC

63   proliferation (Alfonso et al., 2012; Liu et al., 2005), while contact mediated NOTCH signaling

64   between NSCs and TACs regulates NSC quiescence (Kawaguchi et al., 2013). WNT signaling is

65   also known to play a crucial role in orchestrating proliferation and differentiation of adult V-SVZ

66   NSCs (Adachi et al., 2007; Azim et al., 2014; Ortega et al., 2013; Qu et al., 2010; Zywitza et al.,

67   2018). Although these studies provide valuable insights into the significance of WNT signaling in

68   V-SVZ, they do not reveal the key WNT signaling regulators, or a mechanistic understanding of

69   intercellular WNT signaling interactions. Importantly, WNT signaling can be negatively regulated

70   by multiple families of secreted proteins that modulate WNT ligand affinity for the Frizzled

71   receptors of the WNT signaling pathway (reviewed in Driehuis and Clevers, 2017). Therefore;

72   these secreted negative regulators could facilitate adaptive signaling between neuronal

73   progenitors to cope with sustained WNT ligand exposure.

74

75   Highly scalable scRNA-seq technologies (Klein et al., 2015; Macosko et al., 2015; Yuan and Sims,

76   2016; Zheng et al., 2016) have been applied to address cellular heterogeneity and temporal gene

77   expression changes in various stem cell contexts including the V-SVZ field (Mizrak et al., 2019;

78   Tepe et al., 2018; Zywitza et al., 2018); however these V-SVZ studies lacked genetically-induced

79   fate-mapping reporters and could not link V-SVZ NSCs to their progeny in the olfactory bulb.

80   Importantly, current high-throughput methods are unable to link live cell imaging and scRNA-seq

81   data from the same cell, and cannot measure, for example, morphological features of individual

82   cells. Moreover, due to the low sensitivity of large-scale scRNA-seq technologies, many of the

83   expressed transcripts in a given cell are undetected. This is particularly problematic in applications

84   of these technologies to stem cells, where an intracellular reporter or a surface marker is often

85   used to label cells. In this study, we applied large-scale scRNA-seq and an improved version of

86   SCOPE-seq (Yuan et al., 2018), which directly links live-cell imaging and scRNA-seq, to reveal

87   the cellular dynamics of adult neurogenesis. Importantly, we uncovered a rare intermediate

88   population marked by NOTUM, which we demonstrate to be a key mediator of V-SVZ intercellular

89   signaling.

90

91   **RESULTS**

92   **Large-Scale Single Cell Profiling of Adult Mouse Olfactory Bulb with Fate-mapping**

93   **Reporters**

94   We profiled >56,000 cells from matched V-SVZs and OBs of animals carrying either the well-

95   established *hGFAP::CreERT2; Rosa26^{LSL-TdTomato}* (GCERT2) (Ganat et al., 2006; Mich et al.,

96   2014; Obernier et al., 2018) or a newer V-SVZ enriched *ratNes::FLPOER*; *Rosa26^{FSF-TdTomato}*

97   (NESFLPO) fate-mapping reporter (Lao et al., 2012; Wojcinski et al., 2017) (**Figure 1A, Figure**

98   **S1A**). NESFLPO specifically labels cells on lateral ventricle walls, and robustly generates

99   *TdTomato^+* (*TdTom^+*) OB cells four weeks after tamoxifen induction (**Figure S1B**). We identified

100   ten major OB cell populations including migrating NBs and mature neurons (Levine et al., 2015;

101   Shekhar et al., 2016) (**Figure S1C**). Subclustering of the >4,500 OB neurons revealed nine

102   molecularly distinct subtypes (**Figure 1B**, **Table S1**), although morphological classification of OB

3

103   neurons is more complex and dependent on overlapping markers (reviewed in Nagayama et al.,

104   2014). *TdTom* expression was detected in multiple neuron subtypes (64 *TdTom*^{+} neurons), with

105   ≥50% of *TdTom*^{+} neurons in the abundant Neuron1 and 2 (34 *TdTom*^{+} neurons), while the fraction

106   of *TdTom*^{+} neurons was significantly enriched in Neuron3 and 7 (**Figure 1B**). *Gad1* and *Gad2*

107   expression was widespread in OB neurons supporting their GABAergic identity with weaker

108   expression in NBs (Lledo et al., 2008; Nagayama et al., 2014) (**Figure 1B**).

109

110   Next, we surveyed the Allen Mouse Brain Atlas ISH database for subtype-specific markers to

111   examine subtype distribution in the multilayered OB. Using combinations of markers per subtype,

112   we confirmed enrichment of Neuron1, 2, 8 in the granule cell layer, while Neuron4, 5, 6 markers

113   showed enrichment in the glomerular layer (**Figure 1C, Figure S1D**). Neuron7 and 9 markers

114   were predominantly expressed in the anterior olfactory nucleus and external plexiform layer

115   respectively, and Neuron3 was enriched in the mitral cell layer and the external plexiform-

116   glomerular layer boundary (**Figure 1C**). Consistent with scRNA-seq data, immunostainings

117   validated the TdTom co-localization with subtype-specific markers in their predetermined

118   positions, demonstrating the broad repertoire of OB neurons expressing the fate-mapping reporter

119   (**Figure 1D**).

120

121   **Dissection of neuronal lineage progression revealed novel gene expression features and**

122   **key cellular intermediates**

123   To address the complexity of adult neuronal lineage progression and regulation, we generated

124   force-directed graphical visualizations (Weinreb et al., 2017) of neuronal lineage trajectories from

125   V-SVZ astrocyte clusters to OB neurons both in NESFLPO and GCERT2 (12,334 and 7,903 cells,

126   respectively). The resulting trajectories revealed that V-SVZ and OB NBs co-cluster, and lineage

127   progression is constricted by two developmental transitions (**Figure 2A**, **Table S2**). To identify

128   gene signatures associated with neuronal differentiation stages, we factorized the data with

129   single-cell Hierarchical Poisson Factorization (scHPF) (Levitin et al., 2019), and projected cell

130   scores from different factors onto neuronal lineage trajectories. We identified signatures of two

131   intermediate populations corresponding to factors 2 and 5 (**Figure 2B**, **Table S2, Figure S2A**).

132   In the OB, migrating NBs with high cell scores for factor 5 were marked by *Prokr2* and *Htr3a*,

133   mutants of which impair NB migration to the OB (Garcia-Gonzalez et al., 2017; Wen et al., 2019).

134   *Notum*, which encodes a secreted WNT inhibitor, was the highest-ranked gene in factor 2 and

135   marked the V-SVZ transition between qNSCs and aNSCs. Factor 2 was also enriched for *Ascl1*

136 and *Sfrp1*, which encodes another secreted WNT inhibitor, and was distinctly separated from

137 factor 1, enriched for astrocyte genes such as *Gfap*, *Slc1a3,* and *Cldn10* (**Figure 2B**).

138

139 To highlight markers of the qNSC-aNSC transition, we analyzed genes enriched in astrocyte and

140 aNSC clusters compared to the rest of the lineage, which also revealed *Notum* as a top marker

141 of the intermediate cells (**Figure 2C-D**). *Notum* expression preceded factor 2-enriched *Ascl1*

142 expression in the neuronal lineage suggesting additional heterogeneity (**Figure 2D**). To further

143 investigate the heterogeneity among the intermediate cells, we calculated the pointwise mutual

144 information (PMI), a measure of co-expression, for all gene pairs. As expected, factor 2-enriched

145 genes had high PMIs, but also formed significantly distinct co-expression modules (**Figure S2B**)

146 indicating multistep differentiation in the intermediate population and/or heterogeneity in NSC

147 activation. Importantly, we also observed *Notum* enrichment in V-SVZ endothelial cells (**Figure**

148 **S2C**) consistent with previous reports of NOTUM expression in cerebral cortex endothelial cells

149 (Zhang et al., 2014). Next, we identified canonical pathways enriched in *Notum*^{+} cells in the

150 neuronal lineage (**Table S3**) by single-cell differential expression (SCDE) and gene set

151 enrichment analysis (GSEA) (Kharchenko et al., 2014; Subramanian et al., 2005). Interestingly,

152 G1/S transition gene set was significantly upregulated further suggesting an advanced cell cycle

153 state (**Figure 2E**).

154

155 V-SVZ qNSCs are regionally heterogeneous, generating distinct OB interneuron subtypes

156 depending on their location (reviewed in Chaker et al., 2016; Obernier and Alvarez-Buylla, 2019).

157 We identified several main OB neuron subtypes expressing the fate-mapping reporter; however,

158 it is unknown whether the level of heterogeneity at the gene expression level is preserved along

159 neuronal lineage progression. To formally test this, we calculated the phenotypic volume of each

160 cluster in the lineage trajectory, a metric for cellular heterogeneity (Azizi et al., 2018). Astrocytes

161 formed the most heterogeneous cluster (**Figure 2F**), partly due to the inclusion of qNSCs as well

162 as niche astrocytes in this cluster, while aNSC and TACs were more uniform. We observed an

163 increase in cellular heterogeneity in NBs and OB neurons (**Figure 2F**). An additional non-

164 transcriptional mechanism (e.g. epigenetic memory) may be present in NSCs and TACs to store

165 distinct lineage specification information, and/or the underlying heterogeneity can be masked by

166 cell cycle-related genes. Next, we simply plotted the expression of top markers of neuron

167 subtypes with higher fraction of *TdTom*+ cells (**Table S1, Figure 1B**). Interestingly, transcriptional

168 signatures of neuron subtypes varied in the timing of emergence during the lineage progression.

169 The expression of Neuron2 and 3 markers were enriched in NBs, particularly in OB NBs compared

170   to NSCs and TACs (**Figure 2G**), suggesting an activation of a terminal differentiation program at

171   NB stage, while we did not detect any traces of Neuron9 markers in NBs as expected, as well as

172   the markers of Neuron7 located in anterior olfactory nucleus (**Figure 1B**). Newborn neurons were

173   previously reported in anterior olfactory nucleus (Shapiro et al., 2009) and other olfactory

174   processing areas (Feliciano et al., 2015), however the migration and the maturation status of

175   these cells is not fully clear, and our data suggest a lack of connection between OB NBs and

176   Neuron7.

177

178   **SCOPE-seq profiling reveals a dynamic cell size control along neuronal lineage**

179   **progression and a bias of NOTUM toward proliferating cells**

180   We next sought to determine the spatial arrangement of NOTUM-expressing cells in the V-SVZ.

181   Immunofluorescence revealed strong intracellular NOTUM labeling particularly in the ventral V-

182   SVZ (**Figure 3A, Figure S2D**), consistent with high *Notum* enrichment in that region (Mizrak et

183   al., 2019). Whole-mount staining of the V-SVZ (Mirzadeh et al., 2010; Mirzadeh et al., 2008)

184   showed clear NOTUM labeling on the ventricular surface with partial co-localization between

185   NOTUM and GFAP, which marks V-SVZ qNSCs (**Figure 3B**). To further characterize V-SVZ

186   neuronal lineage cells and the *Notum*⁺ intermediate, we performed SCOPE-seq profiling of >2,500

187   V-SVZ neuronal lineage cells. SCOPE-seq (Yuan et al., 2018) uses optically decodable mRNA

188   capture beads to link imaging of dissociated single cells (e.g. cell size, surface staining, multiplet

189   detection) captured in microwells with their scRNA-seq profiles (**Figure 3C**). The neuronal lineage

190   trajectory generated from SCOPE-seq recapitulated the lineage progression order as well as

191   *Notum* expression in the intermediate population (**Figure 3C**, **Table S1**). When optically decoded

192   cells in the neuronal lineage (737/2888 cells) were analyzed (Gunderson et al., 2004; Yuan et al.,

193   2018), we observed a significant increase in cell size at the early aNSC stage (**Figure 3D**). This

194   imaging-based intermediate stage clearly overlapped with *Notum* expressing cells (**Figure 3D**)

195   suggesting *Notum*⁺ cells represent a critical cell size prior to the actively dividing state. Another

196   significant shift in cell size was observed in the early-to-late NB transition, likely due to cell cycle

197   exit. Given the enrichment of G1/S transition gene signatures in *Notum*⁺ cells, the SCOPE-seq

198   data demonstrates a dynamic cell size control during V-SVZ NSC differentiation, where *Notum*

199   marks activating qNSCs at a critical size primed for cell division.

200

201   As a secreted WNT antagonist, NOTUM is active in the extracellular space (Zhang et al., 2015),

202   but can also be retained at the cell surface via binding to glycosaminoglycans on glypicans

203   (**Figure S3A**) (Kakugawa et al., 2015). We used SCOPE-seq to identify NOTUM-bound optically

204   decoded cells (45/737 cells) in the neuronal lineage based on anti-NOTUM surface labeling

205   (**Figure S3B**). Remarkably, these cells showed enrichment of aNSC and TAC cluster gene

206   signatures compared to astrocytes and NBs (**Figure 3E**). Single-cell level GSEA showed

207   significant enrichment of WNT signaling activity in aNSCs and TACs (**Figure 3F**) and depletion in

208   astrocytes, suggesting actively dividing V-SVZ progenitors as potential targets of secreted WNT

209   inhibitors including NOTUM.

210

211   **Pharmacological NOTUM inhibition causes aberrant adult neurogenesis**

212   Given these findings and the crucial context-dependent roles of WNT signaling in orchestrating

213   proliferation and differentiation in the V-SVZ (Adachi et al., 2007; Azim et al., 2014; Ortega et al.,

214   2013; Qu et al., 2010; Zywitza et al., 2018), we hypothesized that NOTUM plays a critical role in

215   regulating V-SVZ neuronal progenitors. To examine NOTUM function in the V-SVZ, we blocked

216   NOTUM activity using a selective small molecule inhibitor (ABC99) (Suciu et al., 2018). To

217   investigate effects of NOTUM inhibition *ex vivo* on the V-SVZ, we generated organotypic slice

218   cultures from *Nestin-CFP* reporter mice (Mignone et al., 2004; Wojcinski et al., 2017), and treated

219   them with ABC99 or the inactive control compound ABC101 (**Figure 4A**). After five days of

220   continuous small molecule and EGF treatment in serum free media, we observed a ventral V-SVZ

221   expansion with dense branches of proliferating (EdU$^+$) progenitors only in the ABC99 treated

222   slices (**Figure 4B-C, Figure S3C**). Next, ABC99 or ABC101 were intraperitoneally (IP) injected

223   into *Nestin-CFP* mice for three consecutive days to assess the effects of NOTUM inhibition *in vivo*

224   one- and five days post-final injection (1 dpi and 5 dpi) (**Figure 4D**). Systemic ABC99

225   administration showed no obvious adverse effects on animal health, as previously reported

226   (Pentinmikko et al., 2019). To measure NOTUM activity and to ensure systemic treatment leads

227   to blockage of NOTUM activity in the V-SVZ, we used mass spectrometry-based activity-based

228   protein profiling (MS-ABPP) (reviewed in Cravatt et al., 2008), and developed a targeted LC-

229   MS/MS method to detect NOTUM-derived peptides. Using this technique, we detected significant

230   NOTUM activity in the V-SVZ (**Table S5**), and a 40-50% inhibition of V-SVZ NOTUM after ABC99

231   injections (**Figure 4E, Figure S3E**). We confirmed WNT pathway activation in the V-SVZ following

232   NOTUM inhibition via qRT-PCR for *Axin2* at 1 dpi (**Figure S3D**) and observed no difference in

233   cell death in the V-SVZ for either ABC99- and ABC101-administered animals. Immunostainings

234   revealed a robust increase in EdU$^+$ dividing progenitors as well as Doublecortin-expressing

235   (DCX$^+$) NBs in the ABC99-treated animals at 1 dpi (**Figure 4F-G**, **Figure S3F**). The increase in

236   NBs was much higher in the ventral V-SVZ, where NOTUM expression is enriched (**Figure 3A**),

237   forming pockets of irregular NB expansion (**Figure 4B, 4J**). The effect on NB expansion was

7

238   transient and disappeared at 5 dpi (**Figure 4H-I**). Consistent with increased NB levels (**Figure**

239   **4G, 4J**), we observed a noticeable thickening of the V-SVZ dorsal wedge, which houses many

240   migrating progenitors (**Figure 4B, 4K**). In sum, NOTUM mediated WNT signaling inhibition targets

241   NSC progeny and prevents their over-expansion in the V-SVZ.

242

243   **DISCUSSION**

244   Regulation of adult neural stem cells (NSCs) and their progeny is achieved by stringent molecular

245   checkpoints to prevent excessive activation which could result in stem cell depletion or

246   pathological conditions. The adult V-SVZ is continuously bathed in proliferative WNT ligands from

247   cerebrospinal fluid (Lehtinen et al., 2011) and local production in the niche (**Figure S3G**). Most

248   adult V-SVZ NSCs divide symmetrically to either self-renew or differentiate (Obernier et al., 2018),

249   and as a result are more prone to rapid depletion. Therefore, conservative molecular mechanisms

250   must be in place to cope with the proliferative signals in the niche (e.g. WNT ligands) ensuring

251   high-efficiency neurogenesis. We used scRNA-seq and SCOPE-seq to identify a negative

252   regulator of WNT signaling, *Notum*, as a key marker of poised V-SVZ NSCs. We propose that as

253   poised NSCs become activated, they release NOTUM to laterally inhibit NSC progeny in the niche

254   to prevent their uncontrolled expansion (**Figure 4L**), thus likely providing a more favorable

255   environment for their daughter cells.

256

257   Elucidating the factors and signaling mechanisms that mediate the interaction between NSCs and

258   their progeny is essential to develop strategies for mitigating tumor growth or promoting tissue

259   regeneration since pathological conditions drive new V-SVZ derived neurons to migrate to the

260   site of injury (reviewed in Chaker et al., 2016). In this study, we identified an intermediate NSC

261   population from a large-scale scRNA-seq dataset using scHPF (Levitin et al., 2019) to which we

262   attribute a key functional role. Transitioning cells represent the dynamic nature of the V-SVZ

263   niche. Since they are primed to generate multiple progenitors, their communication with the other

264   progenitors in the niche is essential to adapt to impending precursors. Similar strategies may also

265   be employed by stem cell intermediates in other adult tissues and organs ensuring on-demand

266   conservative cell replenishment.

267

268   Our analysis also revealed a profound restructuring of cell morphology during lineage progression

269   with several cell size intermediates. Cell cycle and volume need to be tightly coordinated to

270   maintain cellular homeostasis. Particularly, progression through G1/S and G2/M phases has been

271   shown to be size dependent (R. Jones et al., 2017). It will be important to investigate molecular

8

272 mechanisms underlying the cell size changes during NSC differentiation (e.g. nutritional state,

273 translational activation, circadian clock regulation), whether these changes are reversible in the

274 intermediate populations, and to identify the critical size thresholds NSCs commit to activation or

275 exiting cell cycle. Understanding these mechanisms could offer an artificial means of modulating

276 NSC behavior by regulating their size.

277

278 We defined molecularly distinct OB neuron subtypes and validated the repertoire of V-SVZ-

279 derived OB neuron diversity by using different reporter mice combined with scRNA-seq.

280 Progression along V-SVZ to OB neuronal trajectories based on scRNA-seq data demonstrates a

281 convergence of heterogeneous qNSCs to more uniform aNSC and TAC stages, and a late

282 branching during NB to neuron differentiation. These dynamics suggest an additional level of cell-

283 intrinsic programming, such as epigenetic heterogeneity among V-SVZ NSCs and TACs. For

284 example, diverse sets of transcription factors expressed in regionally distinct qNSCs (reviewed in

285 Chaker et al., 2016) may establish epigenetic memory that is conserved in aNSCs and TACs,

286 which later contributes to a later specification event taking place at NB stage. Future single-cell

287 epigenomic profiling studies of V-SVZ NSCs and their progeny could address this complexity.

288 Importantly, our comprehensive V-SVZ-OB dataset provides a resource to map epigenetic

289 changes onto single-cell gene expression data.

290

291 Finally, SCOPE-seq enables direct imaging of protein surface binding by imaging-based detection

292 of fluorescently labeled cells and avoids flow sorting which significantly reduces cell quality and

293 changes cellular composition, particularly in the brain. Unlike the DNA-barcoded antibody based

294 approach (Stoeckius et al., 2017), SCOPE-seq can be utilized to detect cells expressing

295 intracellular reporters such as lineage tracing markers commonly employed in stem cell studies

296 while simultaneously providing morphological insight, such as cell size. Developmental

297 trajectories in different germinal regions consist of cells with a broad distribution of cell imaging

298 features (e.g. cell size, cell shape, marker expression); therefore SCOPE-seq based single cell

299 expression resources can be utilized to rapidly identify and quantify different stem cell states

300 including the rare cell populations in a tissue of interest, under various physiological conditions.
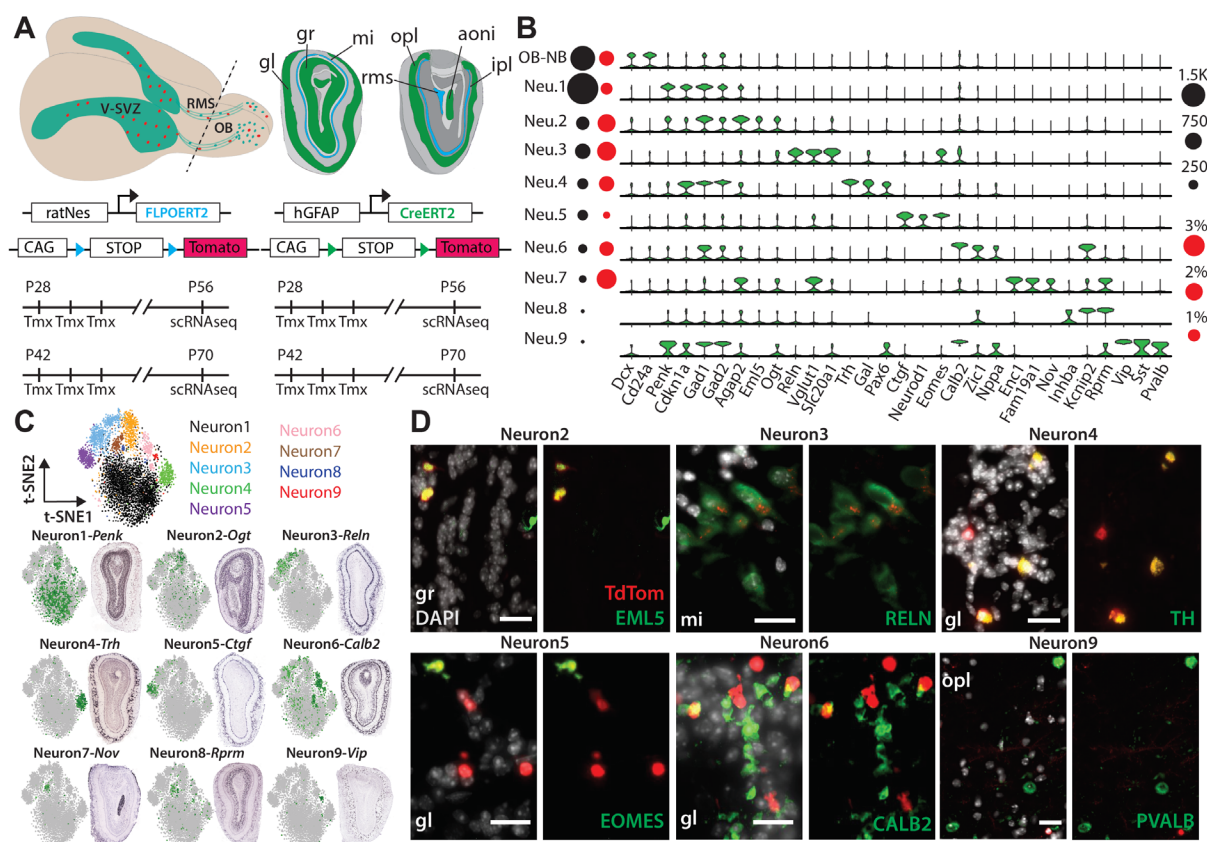
301

302

303

304

305

FIGURES

Figure 1. Fate-mapping experiments and OB Neuron Subtypes. (A) Top: Schema of adult mouse brain (left) showing the migration of V-SVZ neuronal precursors (red) to the OB. Coronal schema (right) highlighting the multi-layered architecture of the OB (gl: glomerular layer, gr: granule cell layer, mi: mitral cell layer, epl: external plexiform layer, ipl: internal plexiform layer, aoni: anterior olfactory nucleus, rms/sez: rostral migratory stream which terminates in the subependymal zone (SEZ) of OB). Bottom: Four and six-week old GCERT2 and NESFLPO animals were injected with tamoxifen for three consecutive days and assayed four weeks after the last injection. **(B)** Violin plots showing $\log_2$(CPM+1) (counts per million) expression values of neuron subtype markers (FDR<0.05). Black and red circles indicate cell numbers and fraction of reporter-positive cells, respectively, in each cluster. **(C)** Top: t-distributed stochastic neighbor embedding (t-SNE) projections of major OB cell types colored separately. Bottom: ISH images showing spatial distribution of subtype markers and their scaled expression on t-SNE. **(D)** Coronal images showing endogenous TdTom and main OB neuron subtype marker co-localization. The corresponding OB layer was indicated on each image. TdTom expression in *mi* layer RELN+ cells was noticeably weaker. Scale bars: 20μm.
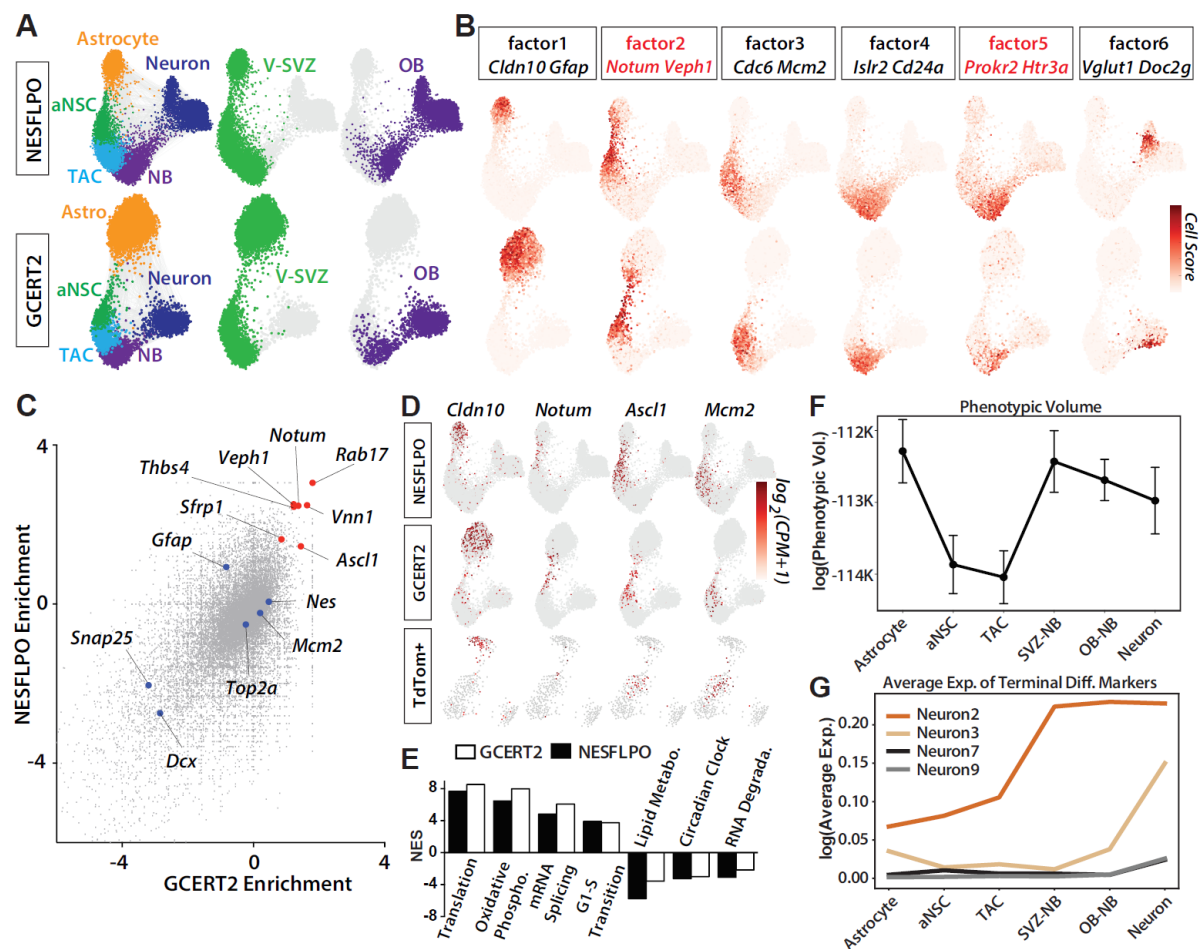
10

Figure 2. Dissection of neuronal lineage progression reveals an intermediate NSC population marked by *Notum* expression. (A) Force-directed neuronal lineage trajectories comprising V-SVZ astrocytes, aNSCs, TACs, and NBs, and OB NBs and neurons both in NESFLPO and GCERT2. Each cell type and/or sample is colored separately. **(B)** Cell scores for six scHPF factors are projected on force-directed lineage trajectories. Two genes with high gene scores are highlighted for each factor. Genes marking the transition states are colored in red. **(C)** GCERT2 and NESFLPO binomial test enrichment of astrocyte and aNSC clusters compared to the remaining neuronal lineage. **(D)** Log_2(CPM+1) expression values of *Cldn10, Notum*, *Ascl1* and *Mcm2* in GCERT2, NESFLPO, TdTom+ cells isolated from GCERT2 and NESFLPO. Cells without marker detection are colored in gray. **(E)** Representative enriched and depleted canonical pathways (FDR < 0.01) in *Notum*+ neuronal lineage cells (NES: Normalized enrichment score). **(F)** Phenotypic volume analysis of different clusters in neuronal lineage. **(G)** Average expression of the top five most specific OB neuron subtype markers in different cell clusters based on the binomial test (FDR < 0.01, Table S1).
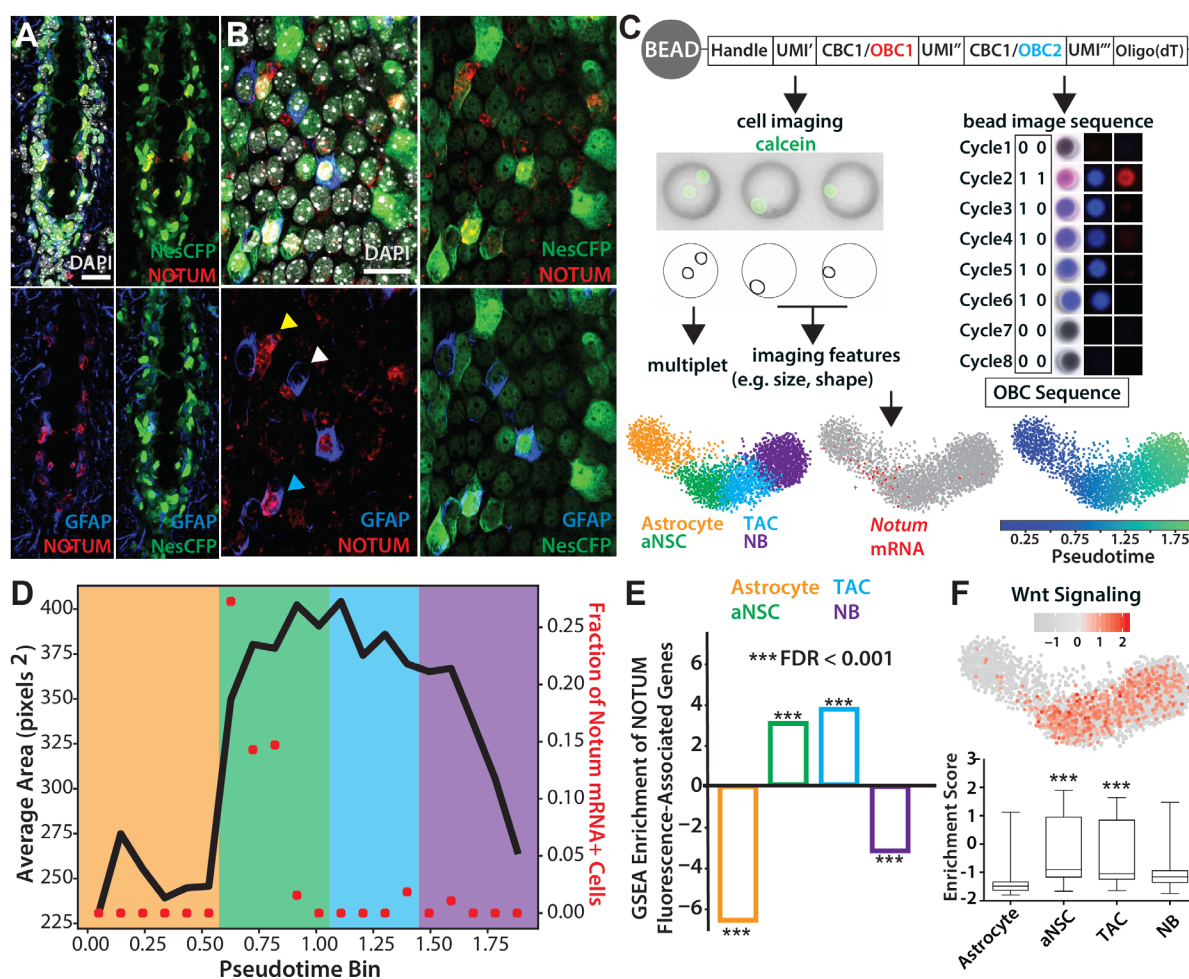
11

338

Figure 3. SCOPE-seq profiling of V-SVZ Neuronal Lineage Cells. (A) Coronal image of ventral
V-SVZ showing NOTUM, NestinCFP (anti-GFP), and GFAP co-localization. Scale bars: 20μm.
(B) Whole-mount staining showing NOTUM reactivity in ventricle contacting cells on the surface
of V-SVZ lateral wall. Cyan arrowhead: NOTUM$^+$GFAP$^+$, white: NOTUM$^-$GFAP$^+$, yellow:
NOTUM$^+$GFAP$^-$ cells. Scale bars: 20μm. **(C)** Top: Workflow for SCOPE-seq using optically
barcoded mRNA capture beads. Following the barcoded cDNA generation, optical demultiplexing
identifies the optical barcode on each bead. Bottom: Pseudotemporal ordering of V-SVZ neuronal
lineage cells, and *Notum* marking astrocyte-aNSC transition. Astrocyte: orange, aNSC: green,
TAC: blue, NB: purple. **(D)** Average size of pseudotemporally ordered neuronal lineage cells and
the fraction of *Notum*+ cells in each pseudotime bin. Shading color corresponds to the stages of
differentiation as labeled in (**C**). **(E)** Enrichment of gene signatures in NOTUM-bound cells in
different cell clusters showing significant enrichment in aNSC and TAC. **(F)** GSEA showing the

351   enrichment or depletion of WNT signaling pathway in individual cells, and the quantification of

352   enrichment scores in each cluster.

353

354

355

356

357

358

359

360

361

362

363

364

365

366

367

368

369

370

371

372

373

374

375
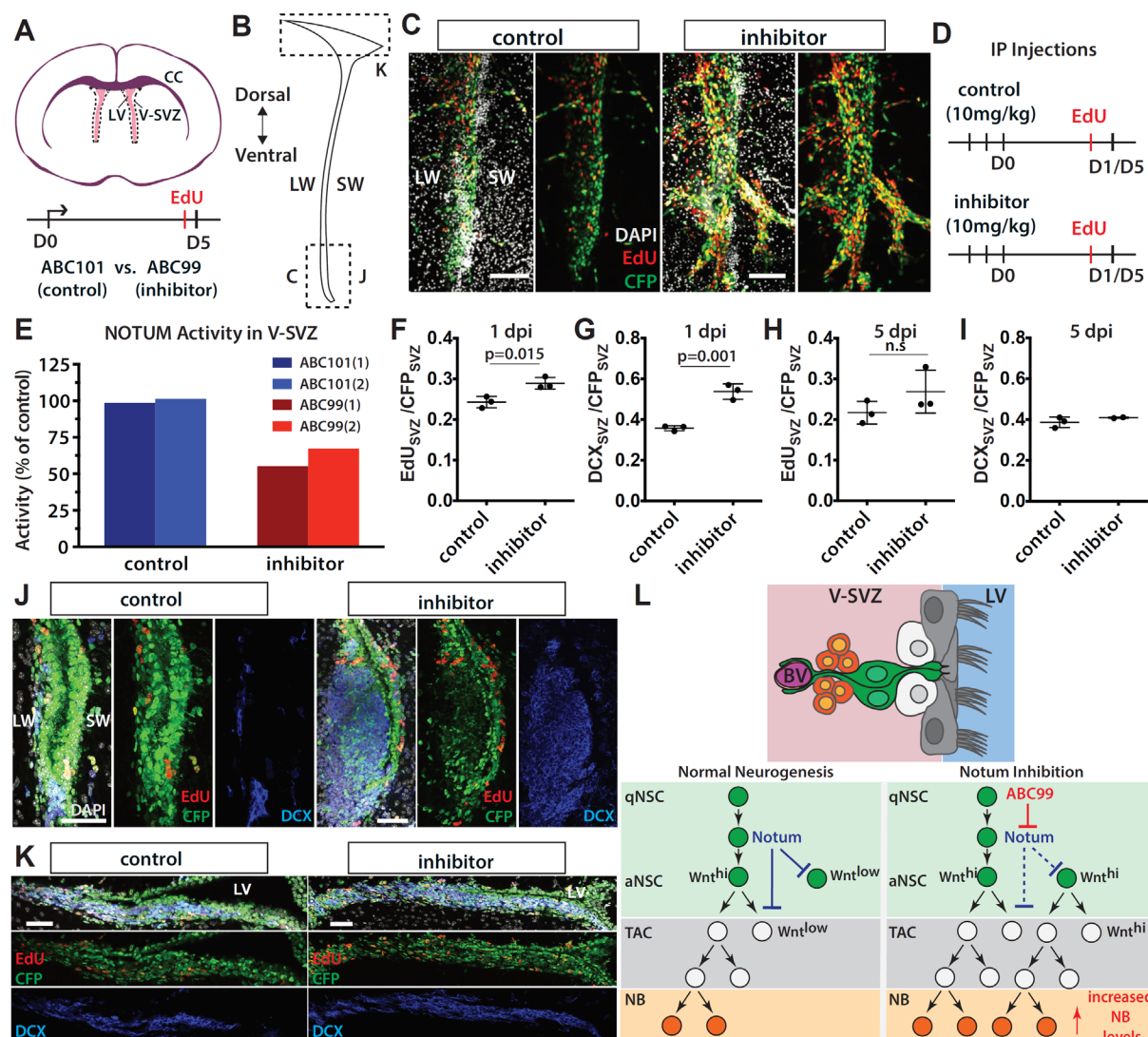
376

377

378

379

380

381

382

383

384

Figure 4. Pharmacological NOTUM inhibition causes aberrant adult neurogenesis. (A) Left: Schema of organotypic slice cultures. Slices were treated with ABC101 or ABC99 for five consecutive days (1 μM each). LV: Lateral Ventricle, LW: Lateral Wall, SW: Septal Wall, CC: Corpus Callosum. **(B)** Coronal schema of V-SVZ showing the location of the images in Figs. 4C, 4J-J. **(C)** Rostro-caudal level matched images of the control or the inhibitor treated V-SVZ slices. Scale bars: 100μm. **(D)** Schema showing IP injection regimen. EdU was injected one hour prior to sacrifice. **(E)** Targeted MS-based ABPP showing reduced NOTUM activity in V-SVZ 4 hours after administration of NOTUM inhibitor ABC99 (10 mg/kg, IP) vs. inactive control ABC101. **(F-I)** Quantification of EdU$^+$/ CFP$^+$ and DCX$^+$/ CFP$^+$ showing a significant increase in NSC progeny in the inhibitor injected animals (n=3 replicates, mean+/-standard deviation(std)) at 1 dpi and a recovery at 5 dpi. **(J)** Representative rostro-caudal level matched images showing the increase

397   in EdU$^+$ and DCX$^+$ cells in the ventral V-SVZ in ABC99-treated animals. NestinCFP (anti-GFP)

398   intensity is stronger in ventricle-contacting NSCs, and ependymal cells, and noticeably weaker in

399   NBs indicating the weak CFP perdurance in NSC progeny. **(K)** Representative dorsal wedge

400   images of V-SVZ. **(L)** Schema of the organization of adult V-SVZ NSCs and their progeny, and a

401   mechanism of NOTUM action in adult neurogenesis (BV: blood vessel).

402

403

404

405

406

407

408

409

410

411

412

413

414

415

416

417

418

419

420

421

422

423

424

425

426

427

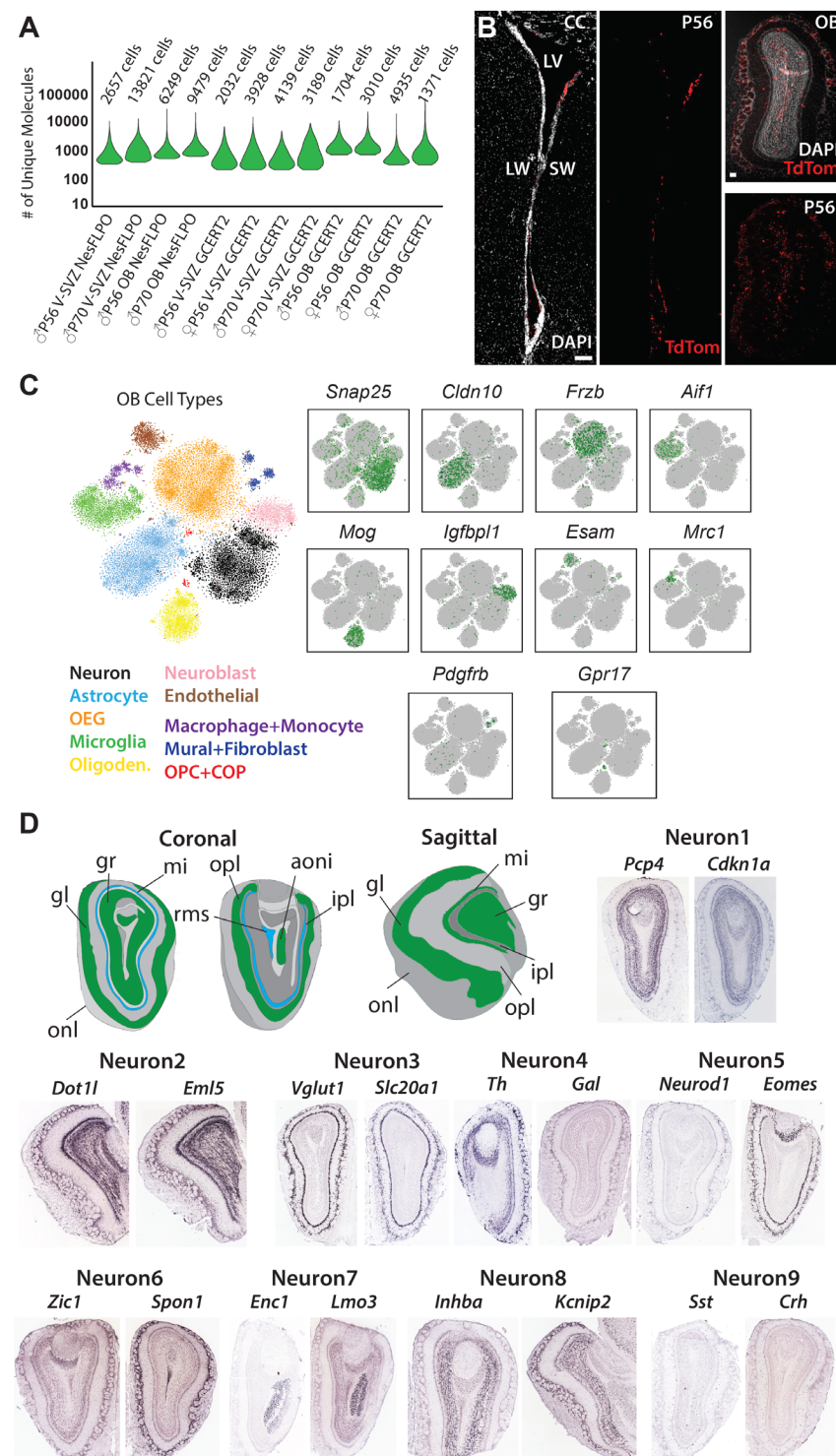428

429

430

431 **SUPPLEMENTARY FIGURES**

Figure S1. (A) Violin plots showing the distribution of unique molecules detected per cell, and the cell numbers in twelve scRNA-seq samples. **(B)** Endogenous TdTom signal in V-SVZ and OB four weeks after tamoxifen injection regimen. TdTom signal is strong even after fixation, and does

16

436 not require immunostainings. Scale bars 100μm. **(C)** t-SNE projections (Van der Maaten and

437 Hinton, 2008) of major OB cell types colored separately (left) and scaled expression of cluster

438 markers (FDR < 0.001). **(D)** ISH data from Allen Mouse Brain Atlas (Lein et al., 2007) (coronal

439 and sagittal sections) showing the spatial distribution of cluster markers used to determine the

440 location of the neuron subtypes.

441

442

443

444

445

446

447

448

449

450

451

452

453

454

455

456

457

458

459

460

461

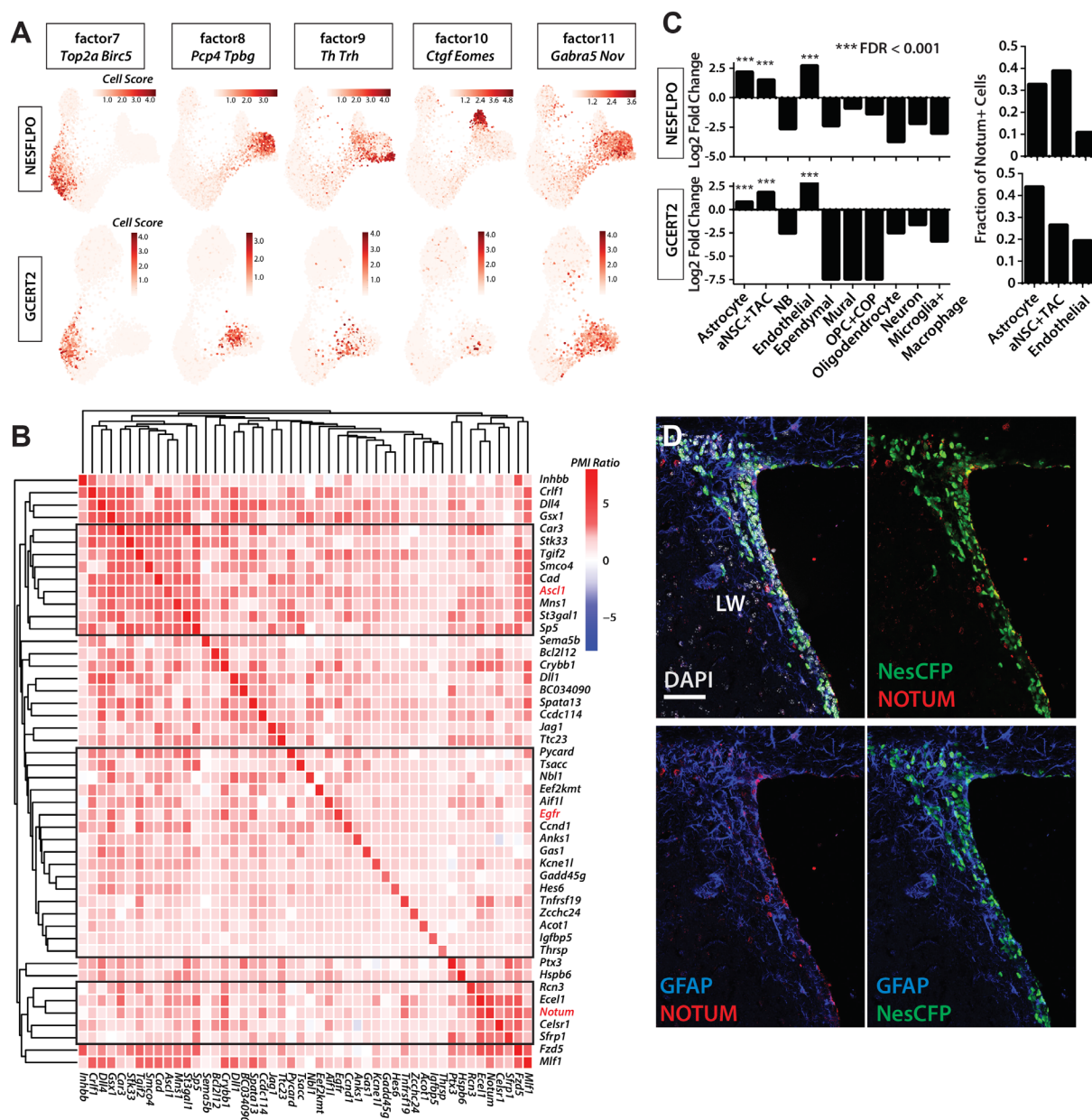462

463

464

465

466

467

468

469

470

471 **Figure S2. (A)** Cell scores for the remaining scHPF factors (**Table S2**) are projected on force-

472 directed lineage trajectories. Two genes with high gene scores are highlighted for each factor. **(B)**

473 Heatmap showing the high co-expression probability ratios of top 50 genes (detected in more

474 than 30 cells) in factor 2, and the significantly different clusters formed by them. Three clusters

475 with more than 2 genes were highlighted in black boxes, and a key identifier gene in each cluster

476 was colored in red. Significant clusters were identified after the removal of an outlier cluster

477 formed by *Olig2* and *Hes5*, resulting in 48 genes in the heatmap. **(C)** Left: Column plot showing

478 the significant enrichment of *Notum* expression in V-SVZ Astrocytes, aNSC+TAC and endothelial

479 cell clusters compared to other V-SVZ cells. *Notum* is significantly depleted in NBs and ventricle

18

480   contacting ependymal cells. Right: The majority of *Notum+* cells in V-SVZ are in astrocyte, aNSC

481   and TAC clusters. **(D)** Coronal images of NOTUM expression in the dorsal V-SVZ. LW: Lateral

482   Wall. Scale bars 50μm.

483

484

485

486

487

488

489

490

491

492

493

494

495

496

497

498

499

500

501

502

503

504

505

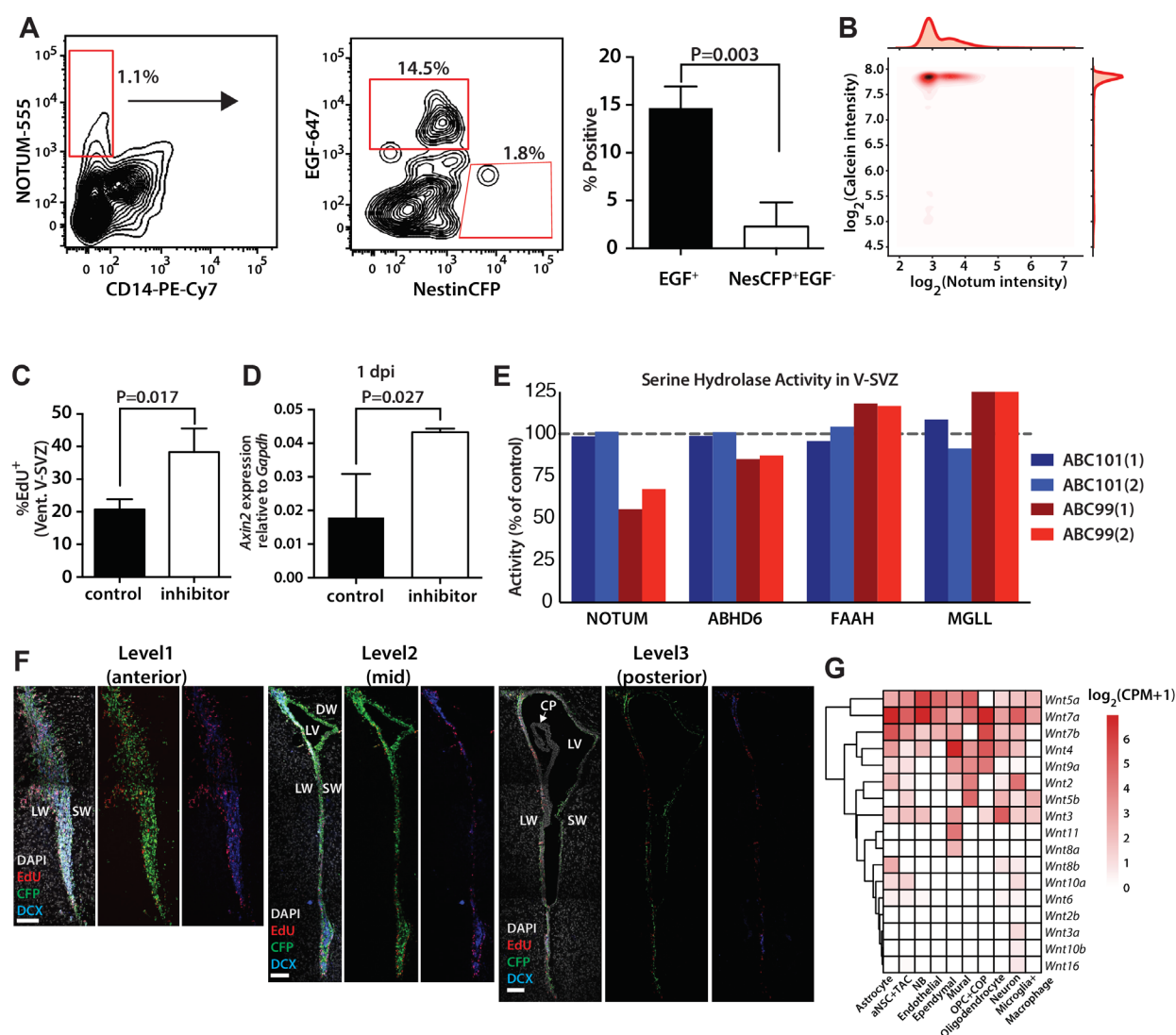506

507

508

509

510

511

512

513

514

515 **Figure S3. (A)** Left: Flow cytometric analysis of NOTUM bound cells showing strong co-labeling

516 with EGF as compared to NestinCFP. Right: Quantification of EGF$^+$, and NestinCFP$^+$EGF$^-$ cell

517 percentages among NOTUM$^+$ cells (n=3 biological replicates, mean+std). EGF-647 was used to

518 label activated NSC progeny (Codega et al., 2014). **(B)** Log transformed Calcein and Notum

519 staining intensities of SCOPE-seq cells. **(C)** Quantification of EdU$^+$ cells in the ventral V-SVZ slice

520 cultures (n=3 sections, mean+std). **(D)** qRT-PCR data indicating *Axin2* upregulation in V-SVZ

521 after the inhibitor injections at 1 dpi (n=3 biological replicates, mean+std). **(E)** Serine hydrolase

522 activity in V-SVZ following ABC101 or ABC99 injections. **(F)** Representative V-SVZ images

523 showing the different rostro-caudal levels analyzed for the quantifications (Level 1: Bregma

524 +1.4mm, Level 2: Bregma +0.9mm, Level 3: Bregma 0.0mm). DW: Dorsal Wall, CP: Choroid

20

525 Plexus. Scale bars 100μm. **(G)** Heatmap showing the average expression (log$_2$(CPM+1)) of WNT

526 ligands in different V-SVZ cell types.

527

528 **SUPPLEMENTARY TABLE LEGENDS**

529

530 **Table S1.** Binomial test results showing the cell type specificity of genes in OB neuron subtypes

531 as well as neuronal lineage cells in GCERT2, NESFLPO and SCOPE-seq datasets. Ensg:

532 Ensemble gene ID. Effect size: log$_2$(fraction of cells in cluster with gene detected/fraction of other

533 cells) FDR: False discovery rate. Related to **Figures 1-3**, **Figure S1**.

534

535 **Table S2.** Gene and cell scores of eleven scHPF factors identified in GCERT2 and NESFLPO.

536 Related to **Figure 2** and **Figure S2**.

537

538 **Table S3.** Differentially expressed genes in *Notum+* cells in GCERT2 and NesFLPO, and

539 preranked GSEA results showing the enrichment or depletion of canonical pathways in *Notum+*

540 cells as compared to the rest of the neuronal lineage cells. Related to **Figure 2**.

541

542 **Table S4.** Oligonucleotide sequences on SCOPE-seq mRNA capture beads. Related to **Figure**

543 **3**.

544

545 **Table S5.** Parallel reaction monitoring results for V-SVZ serine hydrolase activity in ABC101 and

546 ABC99-treated samples. Related to **Figure 4**.

547

548 **EXPERIMENTAL PROCEDURES**

549 *Animals*

550 All experiments were performed according to protocols approved by IACUC at the Columbia

551 University and the Memorial Sloan Kettering Cancer Center. Animals were given access to food

552 and water *ad libitum* and were housed on a 12 hr light/dark cycle, and sacrificed at the same time

553 of day. The following mouse lines were used for the experiments: *Nestin-CFP* (Mignone et al.,

554 2004; Wojcinski et al., 2017), B6.Cg-Tg(GFAP-cre/ERT2)505Fmv/J mice (Stock no: 012849, The

555 Jackson Laboratories) (Ganat et al., 2006), *Nestin-FlpoER* (Lao et al., 2012; Wojcinski et al.,

556 2017), *Rosa26$^{LSL-TdTomato}$* (*Ai14*, Stock: 007909, The Jackson Laboratories), *Rosa26$^{FRT-STOP-FRT-}$*

557 *^{TdTomato}* derived from Ai65 (Stock no: 021875, The Jackson Laboratories), and C57BL/6J (Stock

558 no: 00664, The Jackson Laboratories).

559

560   For *TdTomato* induction, four- or six-weeks old mice were injected with 100 mg/kg of tamoxifen

561   (Sigma) intraperitoneally (IP) for three consecutive days, and sacrificed four weeks after the last

562   injection. ABC99 and ABC101 were injected at 10mg/kg for three consecutive days (Related to

563   **Figure 4**). Subcutaneous EdU (50 mg/kg) injections were done one hour before the animals were

564   sacrificed.

565

566   *Single cell sequencing sample preparation*

567   Whole-mounts of the lateral and septal walls of the V-SVZ were dissected as previously described

568   (Mirzadeh et al., 2010; Mizrak et al., 2019), and combined prior to dissociation. Olfactory bulb

569   (OB) was also removed to profile V-SVZ and OB from the same animal. For scRNA-seq

570   experiments, sex and age of each animal, and the number of single cells analyzed are indicated

571   in the **Figure S1**. Dissected whole mounts were dissociated as described previously (Mizrak et

572   al., 2019). Briefly, minced V-SVZ pieces were digested with papain (Worthington, 6 mg per

573   sample, 10 min at 37°C) in PIPES solution (120 mM NaCl, 5 mM KCl, 20 mM PIPES (Sigma),

574   0.45% glucose, 1x Antibiotic/Antimycotic (Gibco), and phenol red (Sigma) in water; pH adjusted

575   to 7.6). After trituration to single cells in DMEM/F12 containing ovomucoid (Worthington, 0.7

576   mg/ml) and DNAse (Worthington, 0.5 mg/ml), the cell suspension was layered on top of 22%

577   Percoll (Sigma) and centrifuged for 10 mins at 4°C without brakes to remove debris and myelin.

578   The single cell suspension was gently treated with red blood cell lysis buffer (Sigma) for 1 minute,

579   washed by two rounds of centrifugation (1300 rpm at 4°C) and resuspended in 1x Tris Buffered

580   Saline. Cells were stained with Calcein AM live stain dye (Fisher, 1:500) on ice for 30 minutes,

581   and were passed through a 40 μm cell strainer (Fisher) to remove any cell clumps before loading.

582

583   *Single cell library preparation and sequencing*

584   Single cell capture and reverse transcription (RT) were performed as previously described (Yuan

585   and Sims, 2016). Cells were loaded in the microwell devices at a concentration of 400-1000 cells

586   per μl. Cell capture, lysis (2-Mercaptoethanol: Fisher Scientific, Buffer TCL: Qiagen), and reverse

587   transcription (Maxima H Minus Reverse Transcriptase: ThermoFisher, SUPERaseIN:

588   Thermofisher, Template switch oligo: IDT) were all performed on 150K microwell devices

589   (microwell size: x: 50 μm, y: 50 μm, z: 58 μm) controlled by an automated microfluidics system.

590   The devices were scanned on a fluorescence microscope (Eclipse Ti-U, Nikon) during the RNA

591   capture step to check for lysis efficiency. RT reactions were performed on Drop-seq beads

592   (MACOSKO-2011-10, ChemGenes) also captured in the microwells. Beads were collected from

593   the devices and pooled for cDNA amplification step. Following exonuclease I treatment (New

594   England Biolabs), cDNA was amplified by PCR for 14 cycles (KAPA HotStart ReadyMix,

595   Kapabiosystems), and used as input for Nextera tagmentation reactions. cDNA and library quality

596   was assessed using both Qubit and Bioanalyzer (Agilent Technologies). All DNA purification steps

597   were carried out using Ampure XP beads (Beckman). High-quality samples were sequenced on

598   a NextSeq 500 sequencer using a 75 cycle High Output Kit (Illumina, 21 cycle read 1, 63 cycle

599   read 2, and 8 cycle index read).

600

601   *Single cell sequencing data processing and clustering*

602   The sequencing reads were demultiplexed, aligned, and quantified as described previously

603   (Mizrak et al., 2019). Briefly, read 2 was trimmed to remove 3' polyA tails (>7 A's), and fragments

604   with fewer than 24 remaining nucleotides were discarded. Trimmed reads were aligned to the

605   Mus musculus genome and transcriptome annotation (GRCm38, Gencode annotation vM10)

606   using STAR v.2.5.0 with parameters *--sjdbOverhang 65 --twopassMode Basic --outSAMtype BAM*

607   *Unsorted* (Dobin et al., 2013). Only reads with unique, strand-specific alignments to exons were

608   kept for further analysis. *TdTomato* allele was originally designed as tdTomato::WPRE::polyA. As

609   the sequencing data is 3' biased, we used the WPRE sequence with flanking sequences to detect

610   *TdTomato* expression in cells. WPRE is denoted as WRPE in the expression matrices.

611

612   We extracted 12-nt cell barcodes (CBs) and 8-nt unique molecular identifies (UMIs) from read

613   1. Degenerate CBs containing either 'N's or more than four consecutive 'G's were discarded.

614   Synthesis errors, which can result in truncated 11-nt CBs, were corrected similarly to a previously

615   reported method (Shekhar et al., 2016). Briefly, we identified all CBs with at least twenty apparent

616   molecules and for which greater than 90% of UMI-terminal nucleotides were 'T'. These putative

617   truncated CBs were corrected by removing their last nucleotide. This twelfth nucleotide became

618   the new first nucleotide of corresponding UMIs, which were also trimmed of their last ('T') base.

619   We modified our protocol for commercial Drop-seq beads from Chemgenes with a modified

620   structure. A 'V' base was added to the end of the UMI upstream of the poly(T) tail for quality-

621   control purposes. Our analytical pipeline was adjusted to recognize truncated CBs by the

622   presence of excessive 'T' bases one nucleotide downstream of the position used in the previous

623   pipeline. All reads with the same CB, UMI, and gene mapping were collapsed to represent a single

624   molecule. To correct for sequencing errors in UMI's, we further collapsed UMI's that were within

625   Hamming distance 1 of another UMI with the same barcode and gene. To correct for sequencing

626   errors in cell barcodes, we then collapsed CBs that were within Hamming distance one of another

23

627   barcode, had at least 20 unique UMI-gene pairs a piece, and had at least 75% overlap of their

628   UMI-gene pairs. Finally, we repeated UMI error correction and collapse using the error-corrected

629   CBs. The remaining barcode-UMI-gene triplets were used to generate a digital gene expression

630   matrix. The number of cells included in each sample was determined based on the inflection

631   point in the cumulative histograms for molecules as previously described (Macosko et al., 2015;

632   Yuan and Sims, 2016).

633

634   For clustering, we modified our method (Levitin et al., 2019) to select genes detected in fewer

635   cells than expected given their apparent expression level. Briefly, for variable gene selection only,

636   we normalized the molecular counts for each cell to sum to 1. Genes were then ordered by their

637   normalized expression values. For each gene g, we computed a dropout score as follows:

638
$$dropoutscore_g = \frac{|f_g - f_{max,g}|}{\sqrt{f_{max,g}}}$$

639   where f_g is the fraction of cells in the dataset that expressed g, and $f_{max,g}$ is the maximum f_g in a

640   rolling window of 25 genes centered on g. To cluster and visualize the data, we computed a cell

641   by cell Spearman's correlation matrix using the marker genes identified above. Using this matrix,

642   we constructed a k-nearest neighbors graph (k=20), which we then used as input to Louvain

643   clustering with Phenograph (Levine et al., 2015). After clustering, we identified genes most

644   specific to each cluster using a binomial test (Shekhar et al., 2016). The same similarity matrix,

645   transformed into a distance matrix by subtracting its values from 1, was used as input to tSNE for

646   visualization. V-SVZ and OB samples from different genotypes (GCERT2 and NESFLPO) were

647   clustered separately. Astrocyte, aNSC, TAC and NB clusters from V-SVZ, and NB and Neuron

648   clusters from OB were merged and re-clustered (k=20), and the resulting k-nearest neighbors

649   graphs were visualized using force-directed graphs to examine their lineage relationship (Weinreb

650   et al., 2017). Doublets, marked by significant enrichment of canonical markers for more than one

651   cell type (e.g. Astrocyte-Oligodendrocytes, Astrocyte-Neuron) were removed from any analysis.

652   Finally, any contaminating cells (e.g. a small cluster of endothelial cells in the larger neuron

653   cluster) formed separate clusters in the sub-clustering analysis, and were removed from the

654   subsequent analyses.

655

656   *Single cell hierarchical poisson factorization (scHPF), Pointwise Mutual Information (PMI),*

657   *phenotypic volume, differential expression and Gene Set Enrichment (GSEA) analyses*

658   scHPF detects latent factors explaining the discrete expression patterns in the scRNAseq

659   datasets (Levitin et al., 2019). Each gene and cell have a score for each factor demonstrating the

24

660   gene's contribution to the factor, and the factor's contribution to the detected expression in the

661   cell respectively. scHPF was applied to the merged neuronal lineage cells from GCERT2 and

662   NESFLPO using mouse protein coding genes. To select the optimal number of factors, first we

663   ran scHPF for different number of factors, K. For each value of K, we calculated the maximum

664   pairwise overlap of the 100 highest-scoring genes in each factor, and considered overlap

665   significant if $p < 0.05$ by a hypergeometric test. We picked the model with maximum K ($p>0.05$)

666   and identified the factors with consistent expression patterns both in GCERT2 and NESFLPO,

667   which resulted in eleven factors (**Table S2**).

668

669   To assess co-expression and mutual exclusivity of genes, we first identified the significantly

670   expressed genes (detected in more than 30 cells) in the GCERT2 neuronal lineage. For each pair

671   genes, we computed the log-transformed ratio of the joint probability of detecting the two genes

672   in the same cell to the product of their marginal detection probabilities (pointwise mutual

673   information):

674
$$R = \log_2 \frac{P(i,j)}{P(i)P(j)}$$

675

676   Positive values of R indicate co-expression, and negative values indicate mutual exclusivity

677   beyond what would be expected by chance. The results for the top factor 2 genes (**Table S2**)

678   were summarized in **Figure S2B**. Significant clusters of these genes were isolated using R

679   function *pvclust()*, which uses bootstrap resampling to compute p-values (`method.dist=`

680   `"euclidean", method.hclust="average", nboot=1000; alpha=0.95`).

681

682   Phenotypic volume in **Figure 2F** was computed as previously described (Azizi et al., 2018).

683   Briefly, we merged the scRNA-seq count matrices for neuronal lineage cells from the V-SVZ and

684   OB of both the GCERT2 and NESFLPO reporter mice, and applied the Phenograph-based

685   clustering method described above to identify clusters of astrocytes, aNSCs, TACs, neuroblasts,

686   and mature neurons. We transformed the matrix of molecular counts to $\log_2$(counts per

687   thousand+1), including only genes with a >500 total counts in the dataset. We then computed

688   phenotypic volumes for sub-matrices comprised of astrocyte, aSNC, TAC, SVZ-neuroblasts, OB-

689   neuroblasts, or mature neurons as the product of positive eigenvalues of the gene expression

690   covariance matrix for each of the six populations.

691

692   To test the enrichment of WNT signaling pathway (Gene Set M5493-Molecular Signatures

693   Database, Broad Institute) in the SCOPE-seq dataset, we computed the expression of each gene

694   in each cell as the z-scored $\log_2$(counts per million + 1) and produced a ranked list for each cell.

695   GSEA (GSEA v.2.2.2, http://software.broadinstitute.org/gsea/downloads.jsp) was conducted

696   (Subramanian et al., 2005) for the WNT pathway gene set against each ranked list using the Java

697   implementation using the following command:

698   ```
java -cp gsea2-2.2.2.jar -Xmx2512m xtools.gsea.GseaPreranked -scoring_scheme
```

699    ```
classic -setmin 10 -setmax 1000 -nperm 1000
```

700

701   Single-cell differential expression (SCDE) analysis was used to identify differentially expressed

702   genes in *Notum+* cells (Kharchenko et al., 2014). To identify canonical pathways (C2 canonical

703   pathways collection-Broad Institute) enriched or depleted in these cells, SCDE output was pre-

704   ranked based on effect size, and the resulting list was inputted to GSEA using the parameters

705   described above. The results were summarized in **Table S3**.

706

707   *Immunohistochemistry, Microscopy, and Image Analysis*

708   8-10 week-old animals were anesthetized, and transcardially perfused with PBS followed by 4%

709   PFA and brains were post-fixed in 4% PFA for 24 hours. After fixation, brains were treated with

710   30% sucrose until they are embedded in OCT (Tissue-Tek) for cryosectioning. Sections were

711   prepared at 18 μm on cryostat (Leica, CM3050S). Slice cultures were fixed in 4% PFA at end

712   point, and stained at floating sections. Health of the slices were determined based on EdU (Click-

713   IT) incorporation. For immunofluorescent analysis, sections (cryo and slice) were washed with 1X

714   PBS and blocked with blocking buffer (5% BSA in PBS with 0.1% (or 0.3% for slice cultures)

715   Triton-X). Primary antibodies were provided in blocking buffer overnight at 4°C. Washes were

716   performed in PBS with 0.1% Triton-X (or 0.3% for slice cultures). Alexa Fluor conjugated

717   secondary antibodies (Life sciences was supplemented 1/500 in blocking for 1-2 hours at room

718   temperature. After the final washes, EdU staining was performed using Click-IT by manufacturer's

719   protocol. Hoechst 33258 or DAPI (Invitrogen) was used as counter stain. Slides were mounted

720   using Fluorogel Mounting medium (Electron Microscopy Sciences). The following antibodies were

721   used: rat anti-GFP (1:1000, Nacalai Tesque 04404-84), chicken anti-GFAP (1:1000, Abcam

722   ab4674), rabbit anti-NOTUM (1:500, Sigma abs762), goat anti-DCX (1:500, Santa Cruz sc-8066),

723   chicken anti-TH (1:400, Millipore ab9702), mouse anti-RELN (1:200, Millipore mab5364), rabbit

724   anti-EML5 (1:50, hpa054019), rabbit anti-EOMES (1:500, ab23345), rabbit anti-CALB2 (1:200,

725   Millipore ab5054), and mouse anti-PVALB (1:500, mab1572).

726

727 Images were taken using a Zeiss LSM 880 Confocal Microscope or a DM6000 Leica fluorescent

728 microscope. For quantifications, we analyzed sections at three different rostral/caudal levels (from

729 Bregma +1.5 mm to Bregma 0.0 mm) from each replicate (**Figure S3F**). The quantifications from

730 these three levels were averaged to find the total V-SVZ percentages per replicate. Cells in the

731 entire dorsal-ventral extent of V-SVZ were quantified using Fiji software (Schindelin et al., 2012).

732 The identical quantification method was applied to all stainings, replicates and conditions using

733 rostro-caudal level matched sections. Two-way statistical comparisons were conducted using

734 two-tailed unpaired Student's t-test on three biological replicates, which is similar to sample sizes

735 employed in the field. The quantification data was presented as mean+/-standard deviation.

736

737 *Quantitative RT-PCR and Flow Cytometry*

738 ABC99 or ABC101 were injected at 10mg/kg for three consecutive days and the animals were

739 sacrificed at 1 dpi. RNA was isolated from microdissected V-SVZ lateral walls using miRNeasy

740 RNA isolation kit (Qiagen). cDNA was prepared using iScript cDNA preparation kit (BioRad).

741 Following qRT-PCR (Applied BioSystems, Step One) using primers against *Axin2*, relative gene

742 expression levels were quantified using ddCT method. *Gapdh* was used as the housekeeping

743 control to normalize the gene expression. The following primers were used:

744 *Axin2 F 5'-*TGACTCTCCTTCCAGATCCCA-*3'*

745 *Axin2 R 5'-*TGCCCACACTAGGCTGACA-*3'*

746 *Gapdh F 5'-* CCAAGGTGTCCGTCGTGGATCT-*3'*

747 *Gapdh R 5'-* GTTGAAGTCGCAGGAGACAACC-*3'*

748

749 For flow cytometry, V-SVZ lateral walls from 8-10 weeks old *NestinCFP* animals were dissected,

750 and the single cell suspensions were prepared as described above. Following the Percoll

751 gradient, cells were washed by centrifugation (1300 rpm at 4°C). All staining and washes were

752 performed on ice in 1% BSA, 0.1% Glucose HBSS. After each staining step, cells were washed

753 twice by centrifugation (1300 rpm at 4°C). Cells were first incubated in mouse seroblock FcR

754 (1:100, BioRad buf041A) for 10 minutes to avoid non-specific binding of the antibodies. Cells were

755 then incubated for 15 minutes in anti-NOTUM (1:50), followed by Alexa Fluor 555 secondary

756 antibody staining (1:2000). Finally, cells were stained for 15 minutes with PE-Cy7 conjugated rat

757 anti-CD14 (1:50, Biolegend 123315), and Alexa Fluor 647 conjugated EGF (1:250, Thermofisher

758 E35351). At high concentrations, NOTUM antibody non-specifically interacts with Fc receptors on

759 macrophage, monocyte, microglia, lymphocytes, which can be efficiently blocked with the mouse

760 seroblock FcR incubation (nearly 20-fold depletion in $CD14^+$ $NOTUM^+$ cells). After the final

27

761 washes, cells were passed through a 40 μm cell strainer (Fisher) to remove any cell clumps. BD

762 FACS Fortessa was used for flow cytometric analysis, and the data was analyzed using FlowJo.

763 All gates were set using single-color control samples.

764

765 *V-SVZ organotypic Slice Cultures*

766 7-10 week old *NestinCFP/+* animals were euthanized and the brains were dissected into fresh

767 directly into cold HBSS and then embedded in 4% low melting agarose in 1X PBS. Brains were

768 mounted on the chucks and live 250-300um thick coronal sections were obtained using vibratome

769 (Leica). Sections were collected into Neurobasal Media (Invitrogen) supplemented with N2 and

770 B27 Supplements and 20ng/mL EGF (Invitrogen). Sections used for this study spanned the

771 forebrain regions (Bregma +1.4mm to +1mm) Sections were carefully transferred over the

772 membrane inserts (Millipore Millicell cell culture inserts) that are placed over 1mL of media.

773 Alternating sections were treated either with ABC99 or ABC101. Media was changed every day,

774 and 10 ul of media was dropped on each slice to keep them moist. Slices were cultured at 37°C

775 with 5% CO2. Prior to fixation at end point, cultures were pulsed with EdU (2.5μg/mL) for 5 hours.

776

777 *SCOPE-seq sample and library preparation, and sequencing*

778 Single cell suspensions of V-SVZ cells from male C57BL/6J animals were prepared as described

779 above. Following the Percoll gradient, cells were washed in 1% BSA, 0.1% Glucose HBSS by

780 centrifugation (1300 rpm at 4°C). Cells were first incubated in anti-NOTUM (1:50) for 15 minutes

781 on ice, washed twice by centrifugation (1300 rpm at 4°C), and incubated in Alexa Fluor 647

782 secondary antibody (1:2000) for 15 minutes on ice. Cells were then washed twice, and stained

783 with Calcein AM live stain dye (Fisher, 1:500) in 1X TBS on ice for 30 minutes. The resulting cell

784 suspension was passed through a 40 μm cell strainer, and loaded in a microwell device (>130K

785 microwells) at a concentration of 1000 cells per μl. Untrapped cells were flushed out with 1x TBS,

786 and the device was scanned under an inverted automated Nikon Eclipse Ti2 microscope in two

787 fluorescence channels and the bright field channel in ~35 minutes. Optically barcoded (OBC)

788 beads (Chemgenes) were then loaded in the microwell device, and untrapped beads were flushed

789 out with 1x TBS. The microwell device containing the cells and the beads was connected to the

790 computer-controlled reagent and temperature delivery system to perform on-chip RT as described

791 above. The device was scanned during RNA capture to assess the lysis efficiency. After the post-

792 RT washes were completed, the device was disconnected from the automated reagent delivery

793 system. On-chip Exo I treatment was performed at 37°C for 45 minutes followed by TE/TW buffer

794   wash (10 mM Tris pH 8.0, 1 mM EDTA, 0.01% Tween-20). The device was then connected to the

795   automated optical demultiplexing system for reagent delivery.

796

797   Optical demultiplexing was performed as previously described with several modifications (Yuan

798   et al., 2018). Each optically decodable mRNA capture bead is conjugated to an oligonucleotide

799   with two, 8-base sequences, each of which is selected from a different set of 96 sequences (**Table**

800   **S4**). The barcodes are synthesized combinatorially using solid-phase oligonucleotide synthesis

801   (Chemgenes). Together, the two sequences form the cell-identifying barcode for a given bead,

802   and the complete set of cell-identifying barcodes includes 96x96=9,216 possible barcodes.

803   Further multiplexing capacity is achieved by preparing sequencing libraries separately from beads

804   deposited in different sub-arrays of the same device (Yuan et al., 2018). The oligonucleotides

805   also contain interspersed random sequences that form a unique molecular identifier (UMI) and

806   are terminated with poly(dT) to facilitate mRNA capture by hybridization to the poly(A) tail.

807

808   To identify the two sequences on each bead that form the cell-identifying barcode, we use

809   sequential fluorescence hybridization. In each cycle of fluorescence hybridization, we introduce a

810   set of 8-base, Cy5-labeled oligonucleotides to probe the first sequence on each bead and a set

811   of 8-base, Cy3-labeled oligonucleotides to probe the second sequence. The probes are pooled

812   such that all 96 sequences in each set can be identified with eight cycles of sequential

813   fluorescence hybridization (Gunderson et al., 2004) (**Table S4**). Each cycle consists of a

814   background scan and probe scan (two fluorescence channels; Cy3 and Cy5, and bright field), and

815   probe hybridization and stripping (2x SSC buffer with tween-20 and 150mM NaOH melting

816   solution). Background scans showed near absolute probe stripping efficiency. Each pool of

817   hybridization mixture consists of Cy3- and Cy5-labeled oligonucleotides complementary to OBCs

818   (96x96 possible combinations). After the optical demultiplexing workflow, all wells were sealed

819   with perfluorinated oil (Sigma, F3556), the device with separated regions was cut in to 15 pieces

820   with razor blades. Beads from each region were placed in a microcentruge tube containing 100%

821   ethanol, and collected by vortexing, sonication, and centrifugation. By preparing and indexing

822   libraries separately from 15 different device regions, we effectively expand our barcoding capacity

823   to 96x96x15 = 138,240 barcodes. The beads were then washed with TE/SDS (10 mM Tris-HCl,

824   1 mM EDTA, 0.5% SDS) once, TE/TW twice, and nuclease-free water. cDNA was amplified by

825   PCR for 16 cycles (KAPA HotStart ReadyMix, Kapabiosystems), and used as input for Nextera

826   tagmentation reactions. Library preparation was performed as described above resulting in 15

827   sequencing libraries. These libraries were pooled, and sequenced on a NextSeq 500 sequencer

29

828   (Illumina) using a 75 cycle High Output Kit (26 cycle read 1, 58 cycle read 2, and 8 cycle index

829   read).

830

831   *SCOPE-seq imaging and sequencing data analysis*

832   Image analysis was performed using ImageJ. To identify the OBC sequence, each bead was

833   identified in the bright field channel (`setAutoThreshold("Default"); setOption`

834   `("BlackBackground", false); run("Convert to Mask")`), and Cy3 and Cy5 channel

835   intensities were measured in these regions of interest (ROIs). OBC calling was performed using

836   a bead-by-bead algorithm (Gunderson et al., 2004). Cell ROIs were extracted from the cell loading

837   scan using the calcein signal, the intensity measurements were performed for two fluorescence

838   channels (calcein AM and anti-NOTUM fluorescence). The coordinates for the center of the wells

839   and the well ROIs were extracted from the bright field channel (`Auto Local Threshold,`

840   `method=Bernsen, radius=30, parameter_1=40, parameter_2=0`). Cells were assigned

841   to the center of their wells, the wells containing more than one cell were marked as multiplets.

842

843   Both the calcein AM and anti-NOTUM fluorescence intensity distributions were bimodal for

844   microwells containing individual cells (**Figure S3B**). We thresholded the anti-NOTUM and calcein

845   AM fluorescence at the intensity between the two modes of each intensity histogram with the

846   fewest cells to identify a set calcein AM$^+$/NOTUM$^+$ and calcein AM$^+$/NOTUM$^-$ cells for further

847   analysis. We discarded cells for which the same cell-identifying barcode was associated with

848   more than one cell in the same sub-array of the device.

849

850   To analyze the scRNA-seq data from SCOPE-Seq, we first extract the cell-identifying barcode

851   and UMI from Read 1. The sequences in the two sets that are combined to form each cell-

852   identifying barcode have a Hamming distance of at least three for all sequence pairs within each

853   set. Therefore, we correct at most one substitution error in each of the two sequences should one

854   arise from sequencing, oligonucleotide synthesis, or other sources. We only keep reads with a

855   complete cell-identifying barcode. Next, we align the reads from Read 2 using the STAR aligner

856   and keep strand-specific alignments to exons as described above after removing poly(A) tails >7

857   bases long from the 3'-end of each read. Finally, we use the UMIs to estimate the number of

858   molecules associated with each gene in each cell as described above. Clustering and

859   visualization of the scRNA-seq profiles resulting from SCOPE-seq was carried out as described

860   above for conventional scRNA-seq.

861

862   To associate imaging features with pseudotime in the neuronal lineage trajectory, we first
863   extracted neuronal lineage cells from the SCOPE-seq data based on Phenograph clustering of
864   the entire data set. This included all clusters enriched in markers of astrocytes, aNSCs, TACs,
865   and NBs. After marker selection using the drop-out curve for the neuronal lineage cells as
866   described above, we computed a similarity matrix of pairwise Spearman correlation coefficients
867   from which we constructed a k-nearest neighbors graph (k=20) which we projected in two
868   dimensions as a force-directed graph using the *spring_layout* function in the *networkx* Python
869   module. We then fit a polynomial to the resulting two-dimensional projection, which we interpret
870   as the average trajectory. We then assign each cell to a position along this average trajectory by
871   determining its minimum distance from the polynomial curve. Finally, we grouped the cells into 20
872   bins of equal size along the polynomial trajectory to produce **Figure 3D** where we plot the average
873   area (based on calcein AM fluorescence) of the cells in each bin and the fraction of *Notum* mRNA$^+$
874   cells in each bin.

875

876   To associate NOTUM surface staining with gene expression signatures of the four major
877   subpopulations in the neuronal lineage (astrocyte, aNSC, TAC, and NB), we first computed the
878   pointwise mutual information (PMI) between NOTUM surface staining from SCOPE-seq imaging
879   (a categorical where a cell is either positive or negative) and expression of each gene from
880   scRNA-seq (a second categorical where a gene is either detected or not in a given cell):

881
$$R_{NOTUM,g} = \log_2 \left(\frac{P(NOTUM,g)}{P(NOTUM)P(g)} \right)$$

882
883   Here, *P(NOTUM,g)* is the joint probability that a cell is both positive for NOTUM surface staining
884   and positive for detection of the mRNA encoding gene *g*, *P(NOTUM)* is the probability that a cell
885   is positive for NOTUM surface staining, and *P(g)* is the probability that a cell is positive for
886   detection of the mRNA encoding gene *g*. Therefore, if a gene co-occurs with NOTUM surface
887   staining more than expected by chance, $R_{NOTUM,g}$ is positive. To identify genes that were
888   significantly associated with NOTUM surface staining, we used a permutation test, shuffling the
889   identities of NOTUM surface positive cells 1,000 times and correcting the resulting p-values for
890   multiple comparisons using the Benjamini-Hochberg procedure as implemented in the Python
891   module *statsmodels*. We created a gene set comprised of genes detected in greater than 20 cells
892   with $p_{corr} < 0.05$. We then created a ranked list of genes for each of the four neuronal lineage
893   clusters using *-/+log(p)* where *p* is the p-value from the binomial test used to identify genes
894   specific to each cluster that is described above. This parameter is positive for genes that are
895   positively enriched in a given cluster and negative for genes that are depleted. Finally, we used

896   GSEA to compute normalized enrichment scores for the gene set comprised of NOTUM surface

897   staining-associated genes in the ranked list for each of the four clusters using the GSEA

898   parameters described above. The results are summarized in **Figure 3E**.

899

900   *Mass Spectrometry Based Activity-Based Protein Profiling*

901   To prepare V-SVZ proteome, ABC99 or ABC101 were injected at 10mg/kg for three consecutive

902   days and the animals were sacrificed 4 hours after the last injection. Whole-mounts of the lateral

903   wall of V-SVZ were dissected (Mirzadeh et al., 2010) and snap frozen. Frozen samples from each

904   mouse were homogenized using probe sonication in 300 µL of cold DPBS. Protein concentrations

905   were determined using Bio-Rad DC protein assay. Due to the low protein yields, four SVZ

906   proteomes from each group (ABC101 or ABC99-treated) were combined into a single sample and

907   split into two 1.0 mL samples at a protein concentration of 2.7 mg/mL. Tissue homogenates (1.0

908   mL, 2.7 mg/mL) were treated with FP-biotin (10 µL, 1 mM in DMSO) to a final concentration of 10

909   µM and incubated for 1 hour at 37°C with gentle rotation. To remove unreacted probe, protein

910   was precipitated by addition of a cold acetone:methanol (9:1) mixture (8 mL) and incubated at -

911   20°C freezer overnight. The samples were centrifuged at 4,700 x *g* for 15 min at 4°C resulting in

912   the formation of a protein pellet at the bottom of the tube. The supernatant was removed by

913   inversion and the pellet was allowed to air dry for 10 min at room temperature. The protein pellet

914   was dissolved in 0.2 mL of a denaturing solution containing urea (8.0 M), sodium dodecyl sulfate

915   (SDS) (1%), and 1,4-dithiothreitol (DTT) (200 mM) in DPBS. Following complete dissolution, the

916   samples were incubated for 30 min at 37°C and then treated with iodoacetamide (20 µL, 500 mM

917   in DPBS) for an additional 30 min at room temperature. The samples were diluted with 0.25%

918   SDS in DPBS (1.4 mL) and incubated with DPBS-washed streptavidin agarose beads (60 µL) for

919   1 h at room temperature. The streptavidin beads were then sequentially washed with 0.25% SDS

920   (10 x 0.8 mL), DPBS (10 x 1.1 mL), and distilled water (10 x 1.1 mL). The washed beads were

921   transferred to a clean vessel and trypsin (1.6 µg in 100 µl of 2 M urea in DPBS) was added.

922   Samples were incubated overnight at room temperature with agitation. The beads were removed

923   from the digestion using filtration and washed with DPBS (100 µL). The combined filtrates were

924   then acidified by addition of formic acid (20 µL of 100% formic acid) and desalted using SOLAµ™

925   SPE Plates (HRP 2 mg / 1 mL). Samples were dried by centrifugal evaporation and stored at -80

926   °C until analysis.

927

928   Dry peptide samples were reconstituted in water containing 0.1% formic acid (20 µL) and 10 µL

929   were injected onto an EASY-Spray column (15 cm x 75 µm ID, PepMap C18, 3 µm particles, 100

930 Å pore size, Thermo Fisher Scientific) using a Dionex RSLCnano LC (Thermo Fisher Scientific).

931 Peptides were separated over a 30 min gradient of 0 to 40% acetonitrile (0.1% formic acid) and

932 analyzed on an Orbitrap Fusion Lumos (Thermo Fisher Scientific) operated using a parallel

933 reaction monitoring (PRM) method for three distinct NOTUM peptides and a single peptide from

934 three other common serine hydrolase targets: ABHD6, FAAH and MGLL. Selected ions were

935 isolated and fragmented by high energy collision dissociation (HCD) and fragments were detected

936 in the Orbitrap at 15,000 or 30,000 resolution. Sequences, targets and targeting parameters can

937 be found in **Table S5** (PRM Parameters).

938

939 Raw data files were uploaded analyzed in Skyline (v4.2.0.19009) to determine the relative

940 abundance of each serine hydrolase peptide in vehicle-treated samples relative to ABC99-treated

941 samples. Peptide quantification was performed by calculating the sum of the peak areas

942 corresponding to 6 fragment ions from each peptide (see table below). To determine protein

943 activity relative to the controls, an area ratio was calculated for each fragment ion, dividing the

944 peak area of an ABC99-treated sample by the mean peak area of the ABC101-control samples.

945 The relative protein activity was found from the slope of the regression line obtained by plotting

946 the treated ratios against mean control ratios. The peptides and fragment ions were pre-selected

947 from in-house reference spectral libraries acquired in data-dependent acquisition mode to identify

948 authentic spectra for each peptide. Product ions used for Skyline quantification appear in **Table

949 S5**.

950

954

955 **Author Contributions:** D.M. and P.A.S. designed the study. D.M. performed the scRNA-seq

956 and SCOPE-seq experiments. D.M. and P.A.S. analyzed the data. D.M. and N.S.B. performed

957 the immunostainings and the functional validation experiments. J.Y., Z.L., and P.A.S. developed

958 SCOPE-seq. R.S., M.J.N., N.N., K.M.L and B.F.C. performed and analyzed MS-ABPP

959 experiments. D.M., N.S.B., M.J.N., A.L.J., and P.A.S. wrote the manuscript.

960

961 **Competing Interests:** Columbia University has filed patent applications on SCOPE-seq, and

962 P.A.S. and J.Y. are listed as inventors.

963

33

Data Availability: The sequencing data and count matrices have been deposited with the Gene Expression Omnibus (GEO) under accession code GSE134918.

Code Availability: Data analysis code used for scRNA-seq is available at https://github.com/simslab.

REFERENCES

Adachi, K., Mirzadeh, Z., Sakaguchi, M., Yamashita, T., Nikolcheva, T., Gotoh, Y., Peltz, G., Gong, L., Kawase, T., Alvarez-Buylla, A.*, et al.* (2007). Beta-catenin signaling promotes proliferation of progenitor cells in the adult mouse subventricular zone. Stem Cells *25*, 2827-2836.

Alfonso, J., Le Magueresse, C., Zuccotti, A., Khodosevich, K., and Monyer, H. (2012). Diazepam binding inhibitor promotes progenitor proliferation in the postnatal SVZ by reducing GABA signaling. Cell Stem Cell *10*, 76-87.

Azim, K., Fischer, B., Hurtado-Chong, A., Draganova, K., Cantu, C., Zemke, M., Sommer, L., Butt, A., and Raineteau, O. (2014). Persistent Wnt/beta-catenin signaling determines dorsalization of the postnatal subventricular zone and neural stem cell specification into oligodendrocytes and glutamatergic neurons. Stem Cells *32*, 1301-1312.

Azizi, E., Carr, A.J., Plitas, G., Cornish, A.E., Konopacki, C., Prabhakaran, S., Nainys, J., Wu, K., Kiseliovas, V., Setty, M.*, et al.* (2018). Single-Cell Map of Diverse Immune Phenotypes in the Breast Tumor Microenvironment. Cell *174*, 1293-1308 e1236.

Brill, M.S., Ninkovic, J., Winpenny, E., Hodge, R.D., Ozen, I., Yang, R., Lepier, A., Gascon, S., Erdelyi, F., Szabo, G.*, et al.* (2009). Adult generation of glutamatergic olfactory bulb interneurons. Nat Neurosci *12*, 1524-1533.

Chaker, Z., Codega, P., and Doetsch, F. (2016). A mosaic world: puzzles revealed by adult neural stem cell heterogeneity. Wiley Interdiscip Rev Dev Biol *5*, 640-658.

Codega, P., Silva-Vargas, V., Paul, A., Maldonado-Soto, A.R., Deleo, A.M., Pastrana, E., and Doetsch, F. (2014). Prospective identification and purification of quiescent adult neural stem cells from their in vivo niche. Neuron *82*, 545-559.

Cravatt, B.F., Wright, A.T., and Kozarich, J.W. (2008). Activity-based protein profiling: from enzyme chemistry to proteomic chemistry. Annu Rev Biochem *77*, 383-414.

Delgado, R.N., and Lim, D.A. (2015). Embryonic Nkx2.1-expressing neural precursor cells contribute to the regional heterogeneity of adult V-SVZ neural stem cells. Dev Biol *407*, 265-274.

999   Dobin, A., Davis, C.A., Schlesinger, F., Drenkow, J., Zaleski, C., Jha, S., Batut, P., Chaisson,

1000   M., and Gingeras, T.R. (2013). STAR: ultrafast universal RNA-seq aligner. Bioinformatics

1001   (Oxford, England) *29*, 15-21.

1002   Doetsch, F., Caille, I., Lim, D.A., Garcia-Verdugo, J.M., and Alvarez-Buylla, A. (1999).

1003   Subventricular zone astrocytes are neural stem cells in the adult mammalian brain. Cell *97*, 703-

1004   716.

1005   Driehuis, E., and Clevers, H. (2017). WNT signalling events near the cell membrane and their

1006   pharmacological targeting for the treatment of cancer. Br J Pharmacol *174*, 4547-4563.

1007   Eng, C.L., Lawson, M., Zhu, Q., Dries, R., Koulena, N., Takei, Y., Yun, J., Cronin, C., Karp, C.,

1008   Yuan, G.C.*, et al.* (2019). Transcriptome-scale super-resolved imaging in tissues by RNA

1009   seqFISH. Nature *568*, 235-239.

1010   Feliciano, D.M., Bordey, A., and Bonfanti, L. (2015). Noncanonical Sites of Adult Neurogenesis

1011   in the Mammalian Brain. Cold Spring Harb Perspect Biol *7*, a018846.

1012   Fiorelli, R., Azim, K., Fischer, B., and Raineteau, O. (2015). Adding a spatial dimension to

1013   postnatal ventricular-subventricular zone neurogenesis. Development *142*, 2109-2120.

1014   Fuentealba, L.C., Rompani, S.B., Parraguez, J.I., Obernier, K., Romero, R., Cepko, C.L., and

1015   Alvarez-Buylla, A. (2015). Embryonic Origin of Postnatal Neural Stem Cells. Cell *161*, 1644-

1016   1655.

1017   Ganat, Y.M., Silbereis, J., Cave, C., Ngu, H., Anderson, G.M., Ohkubo, Y., Ment, L.R., and

1018   Vaccarino, F.M. (2006). Early postnatal astroglial cells produce multilineage precursors and

1019   neural stem cells in vivo. J Neurosci *26*, 8609-8621.

1020   Garcia-Gonzalez, D., Khodosevich, K., Watanabe, Y., Rollenhagen, A., Lubke, J.H.R., and

1021   Monyer, H. (2017). Serotonergic Projections Govern Postnatal Neuroblast Migration. Neuron *94*,

1022   534-549 e539.

1023   Gunderson, K.L., Kruglyak, S., Graige, M.S., Garcia, F., Kermani, B.G., Zhao, C., Che, D.,

1024   Dickinson, T., Wickham, E., Bierle, J.*, et al.* (2004). Decoding randomly ordered DNA arrays.

1025   Genome Res *14*, 870-877.

1026   Kakugawa, S., Langton, P.F., Zebisch, M., Howell, S., Chang, T.H., Liu, Y., Feizi, T., Bineva, G.,

1027   O'Reilly, N., Snijders, A.P.*, et al.* (2015). Notum deacylates Wnt proteins to suppress signalling

1028   activity. Nature *519*, 187-192.

1029   Kawaguchi, D., Furutachi, S., Kawai, H., Hozumi, K., and Gotoh, Y. (2013). Dll1 maintains

1030   quiescence of adult neural stem cells and segregates asymmetrically during mitosis. Nat

1031   Commun *4*, 1880.

1032   Kharchenko, P.V., Silberstein, L., and Scadden, D.T. (2014). Bayesian approach to single-cell

1033   differential expression analysis. Nature methods *11*, 740-742.

1034   Klein, A.M., Mazutis, L., Akartuna, I., Tallapragada, N., Veres, A., Li, V., Peshkin, L., Weitz,

1035   D.A., and Kirschner, M.W. (2015). Droplet barcoding for single-cell transcriptomics applied to

1036   embryonic stem cells. Cell *161*, 1187-1201.

1037   Kohwi, M., Osumi, N., Rubenstein, J.L., and Alvarez-Buylla, A. (2005). Pax6 is required for

1038   making specific subpopulations of granule and periglomerular neurons in the olfactory bulb. J

1039   Neurosci *25*, 6997-7003.

1040   Kriegstein, A., and Alvarez-Buylla, A. (2009). The glial nature of embryonic and adult neural

1041   stem cells. Annu Rev Neurosci *32*, 149-184.

1042   Lao, Z., Raju, G.P., Bai, C.B., and Joyner, A.L. (2012). MASTR: a technique for mosaic mutant

1043   analysis with spatial and temporal control of recombination using conditional floxed alleles in

1044   mice. Cell Rep *2*, 386-396.

1045   Lehtinen, M.K., Zappaterra, M.W., Chen, X., Yang, Y.J., Hill, A.D., Lun, M., Maynard, T.,

1046   Gonzalez, D., Kim, S., Ye, P.*, et al.* (2011). The cerebrospinal fluid provides a proliferative niche

1047   for neural progenitor cells. Neuron *69*, 893-905.

1048   Lein, E.S., Hawrylycz, M.J., Ao, N., Ayres, M., Bensinger, A., Bernard, A., Boe, A.F., Boguski,

1049   M.S., Brockway, K.S., Byrnes, E.J.*, et al.* (2007). Genome-wide atlas of gene expression in the

1050   adult mouse brain. Nature *445*, 168-176.

1051   Levine, J.H., Simonds, E.F., Bendall, S.C., Davis, K.L., Amir el, A.D., Tadmor, M.D., Litvin, O.,

1052   Fienberg, H.G., Jager, A., Zunder, E.R.*, et al.* (2015). Data-Driven Phenotypic Dissection of

1053   AML Reveals Progenitor-like Cells that Correlate with Prognosis. Cell *162*, 184-197.

1054   Levitin, H.M., Yuan, J., Cheng, Y.L., Ruiz, F.J., Bush, E.C., Bruce, J.N., Canoll, P., Iavarone, A.,

1055   Lasorella, A., Blei, D.M.*, et al.* (2019). De novo gene signature identification from single-cell

1056   RNA-seq with hierarchical Poisson factorization. Mol Syst Biol *15*, e8557.

1057   Liu, X., Wang, Q., Haydar, T.F., and Bordey, A. (2005). Nonsynaptic GABA signaling in

1058   postnatal subventricular zone controls proliferation of GFAP-expressing progenitors. Nat

1059   Neurosci *8*, 1179-1187.

1060   Lledo, P.M., Merkle, F.T., and Alvarez-Buylla, A. (2008). Origin and function of olfactory bulb

1061   interneuron diversity. Trends Neurosci *31*, 392-400.

1062   Lopez-Juarez, A., Howard, J., Ullom, K., Howard, L., Grande, A., Pardo, A., Waclaw, R., Sun,

1063   Y.Y., Yang, D., Kuan, C.Y.*, et al.* (2013). Gsx2 controls region-specific activation of neural stem

1064   cells and injury-induced neurogenesis in the adult subventricular zone. Genes Dev *27*, 1272-

1065   1287.

1066   Macosko, E.Z., Basu, A., Satija, R., Nemesh, J., Shekhar, K., Goldman, M., Tirosh, I., Bialas,

1067   A.R., Kamitaki, N., Martersteck, E.M*., et al.* (2015). Highly Parallel Genome-wide Expression

1068   Profiling of Individual Cells Using Nanoliter Droplets. Cell *161*, 1202-1214.

1069   Merkle, F.T., Fuentealba, L.C., Sanders, T.A., Magno, L., Kessaris, N., and Alvarez-Buylla, A.

1070   (2014). Adult neural stem cells in distinct microdomains generate previously unknown

1071   interneuron types. Nat Neurosci *17*, 207-214.

1072   Merkle, F.T., Mirzadeh, Z., and Alvarez-Buylla, A. (2007). Mosaic organization of neural stem

1073   cells in the adult brain. Science *317*, 381-384.

1074   Mich, J.K., Signer, R.A., Nakada, D., Pineda, A., Burgess, R.J., Vue, T.Y., Johnson, J.E., and

1075   Morrison, S.J. (2014). Prospective identification of functionally distinct stem cells and

1076   neurosphere-initiating cells in adult mouse forebrain. Elife *3*, e02669.

1077   Mignone, J.L., Kukekov, V., Chiang, A.S., Steindler, D., and Enikolopov, G. (2004). Neural stem

1078   and progenitor cells in nestin-GFP transgenic mice. J Comp Neurol *469*, 311-324.

1079   Mirzadeh, Z., Doetsch, F., Sawamoto, K., Wichterle, H., and Alvarez-Buylla, A. (2010). The

1080   subventricular zone en-face: wholemount staining and ependymal flow. J Vis Exp.

1081   Mirzadeh, Z., Merkle, F.T., Soriano-Navarro, M., Garcia-Verdugo, J.M., and Alvarez-Buylla, A.

1082   (2008). Neural stem cells confer unique pinwheel architecture to the ventricular surface in

1083   neurogenic regions of the adult brain. Cell Stem Cell *3*, 265-278.

1084   Mizrak, D., Levitin, H.M., Delgado, A.C., Crotet, V., Yuan, J., Chaker, Z., Silva-Vargas, V., Sims,

1085   P.A., and Doetsch, F. (2019). Single-Cell Analysis of Regional Differences in Adult V-SVZ

1086   Neural Stem Cell Lineages. Cell Rep *26*, 394-406 e395.

1087   Nagayama, S., Homma, R., and Imamura, F. (2014). Neuronal organization of olfactory bulb

1088   circuits. Front Neural Circuits *8*, 98.

1089   Obernier, K., and Alvarez-Buylla, A. (2019). Neural stem cells: origin, heterogeneity and

1090   regulation in the adult mammalian brain. Development *146*.

1091   Obernier, K., Cebrian-Silla, A., Thomson, M., Parraguez, J.I., Anderson, R., Guinto, C., Rodas

1092   Rodriguez, J., Garcia-Verdugo, J.M., and Alvarez-Buylla, A. (2018). Adult Neurogenesis Is

1093   Sustained by Symmetric Self-Renewal and Differentiation. Cell Stem Cell *22*, 221-234 e228.

1094   Ortega, F., Gascon, S., Masserdotti, G., Deshpande, A., Simon, C., Fischer, J., Dimou, L.,

1095   Chichung Lie, D., Schroeder, T., and Berninger, B. (2013). Oligodendrogliogenic and

1096   neurogenic adult subependymal zone neural stem cells constitute distinct lineages and exhibit

1097   differential responsiveness to Wnt signalling. Nat Cell Biol *15*, 602-613.

1098   Pentinmikko, N., Iqbal, S., Mana, M., Andersson, S., Cognetta, A.B., 3rd, Suciu, R.M., Roper, J.,

1099   Luopajarvi, K., Markelin, E., Gopalakrishnan, S.*, et al.* (2019). Notum produced by Paneth cells

1100   attenuates regeneration of aged intestinal epithelium. Nature.

1101   Qu, Q., Sun, G., Li, W., Yang, S., Ye, P., Zhao, C., Yu, R.T., Gage, F.H., Evans, R.M., and Shi,

1102   Y. (2010). Orphan nuclear receptor TLX activates Wnt/beta-catenin signalling to stimulate

1103   neural stem cell proliferation and self-renewal. Nat Cell Biol *12*, 31-40; sup pp 31-39.

1104   R. Jones, A., Forero-Vargas, M., Withers, S.P., Smith, R.S., Traas, J., Dewitte, W., and Murray,

1105   J.A.H. (2017). Cell-size dependent progression of the cell cycle creates homeostasis and

1106   flexibility of plant cell size. Nat Commun *8*, 15060.

1107   Schindelin, J., Arganda-Carreras, I., Frise, E., Kaynig, V., Longair, M., Pietzsch, T., Preibisch,

1108   S., Rueden, C., Saalfeld, S., Schmid, B.*, et al.* (2012). Fiji: an open-source platform for

1109   biological-image analysis. Nat Methods *9*, 676-682.

1110   Shapiro, L.A., Ng, K., Zhou, Q.Y., and Ribak, C.E. (2009). Subventricular zone-derived, newly

1111   generated neurons populate several olfactory and limbic forebrain regions. Epilepsy Behav *14

1112   Suppl 1*, 74-80.

1113   Shekhar, K., Lapan, S.W., Whitney, I.E., Tran, N.M., Macosko, E.Z., Kowalczyk, M., Adiconis,

1114   X., Levin, J.Z., Nemesh, J., Goldman, M.*, et al.* (2016). Comprehensive Classification of Retinal

1115   Bipolar Neurons by Single-Cell Transcriptomics. Cell *166*, 1308-1323 e1330.

1116   Stoeckius, M., Hafemeister, C., Stephenson, W., Houck-Loomis, B., Chattopadhyay, P.K.,

1117   Swerdlow, H., Satija, R., and Smibert, P. (2017). Simultaneous epitope and transcriptome

1118   measurement in single cells. Nat Methods *14*, 865-868.

1119   Subramanian, A., Tamayo, P., Mootha, V.K., Mukherjee, S., Ebert, B.L., Gillette, M.A.,

1120   Paulovich, A., Pomeroy, S.L., Golub, T.R., Lander, E.S.*, et al.* (2005). Gene set enrichment

1121   analysis: a knowledge-based approach for interpreting genome-wide expression profiles. Proc

1122   Natl Acad Sci U S A *102*, 15545-15550.

1123   Suciu, R.M., Cognetta, A.B., 3rd, Potter, Z.E., and Cravatt, B.F. (2018). Selective Irreversible

1124   Inhibitors of the Wnt-Deacylating Enzyme NOTUM Developed by Activity-Based Protein

1125   Profiling. ACS Med Chem Lett *9*, 563-568.

1126   Tepe, B., Hill, M.C., Pekarek, B.T., Hunt, P.J., Martin, T.J., Martin, J.F., and Arenkiel, B.R.

1127   (2018). Single-Cell RNA-Seq of Mouse Olfactory Bulb Reveals Cellular Heterogeneity and

1128   Activity-Dependent Molecular Census of Adult-Born Neurons. Cell Rep *25*, 2689-2703 e2683.

1129   Van der Maaten, L., and Hinton, G. (2008). Visualizing Data using t-SNE. Journal of Machine

1130   Learning Research *9*, 2579-2605.

1131 Weinreb, C., Wolock, S., and Klein, A. (2017). SPRING: a kinetic interface for visualizing high

1132 dimensional single-cell expression data. Bioinformatics.

1133 Wen, Y., Zhang, Z., Li, Z., Liu, G., Tao, G., Song, X., Xu, Z., Shang, Z., Guo, T., Su, Z., *et al.*

1134 (2019). The PROK2/PROKR2 signaling pathway is required for the migration of most olfactory

1135 bulb interneurons. J Comp Neurol.

1136 Wojcinski, A., Lawton, A.K., Bayin, N.S., Lao, Z., Stephen, D.N., and Joyner, A.L. (2017).

1137 Cerebellar granule cell replenishment postinjury by adaptive reprogramming of Nestin(+)

1138 progenitors. Nat Neurosci *20*, 1361-1370.

1139 Yuan, J., Sheng, J., and Sims, P.A. (2018). SCOPE-Seq: a scalable technology for linking live

1140 cell imaging and single-cell RNA sequencing. Genome Biol *19*, 227.

1141 Yuan, J., and Sims, P.A. (2016). An Automated Microwell Platform for Large-Scale Single Cell

1142 RNA-Seq. Sci Rep *6*, 33883.

1143 Zhang, X., Cheong, S.M., Amado, N.G., Reis, A.H., MacDonald, B.T., Zebisch, M., Jones, E.Y.,

1144 Abreu, J.G., and He, X. (2015). Notum is required for neural and head induction via Wnt

1145 deacylation, oxidation, and inactivation. Dev Cell *32*, 719-730.

1146 Zhang, Y., Chen, K., Sloan, S.A., Bennett, M.L., Scholze, A.R., O'Keeffe, S., Phatnani, H.P.,

1147 Guarnieri, P., Caneda, C., Ruderisch, N.*, et al.* (2014). An RNA-sequencing transcriptome and

1148 splicing database of glia, neurons, and vascular cells of the cerebral cortex. J Neurosci *34*,

1149 11929-11947.

1150 Zheng, G.X., Lau, B.T., Schnall-Levin, M., Jarosz, M., Bell, J.M., Hindson, C.M., Kyriazopoulou-

1151 Panagiotopoulou, S., Masquelier, D.A., Merrill, L., Terry, J.M.*, et al.* (2016). Haplotyping

1152 germline and cancer genomes with high-throughput linked-read sequencing. Nat Biotechnol *34*,

1153 303-311.

1154 Zweifel, S., Marcy, G., Lo Guidice, Q., Li, D., Heinrich, C., Azim, K., and Raineteau, O. (2018).

1155 HOPX Defines Heterogeneity of Postnatal Subventricular Zone Neural Stem Cells. Stem Cell

1156 Reports *11*, 770-783.

1157 Zywitza, V., Misios, A., Bunatyan, L., Willnow, T.E., and Rajewsky, N. (2018). Single-Cell

1158 Transcriptomics Characterizes Cell Types in the Subventricular Zone and Uncovers Molecular

1159 Defects Impairing Adult Neurogenesis. Cell Rep *25*, 2457-2469 e2458.

1160